Romanian Reports in Physics, Vol. 68, Supplement, P. S735–S797, 2016

POSITRON PRODUCTION BY GAMMA BEAM AT ELI–NP

N. DJOURELOV[1,*], C. HUGENSCHMIDT[2], S. BALASCUTA[1], V. LECA[1], A. OPRISA[1], C. PIOCHACZ[2], C. TEODORESCU[3], C. A. UR[1]

[1]ELI-NP, "Horia Hulubei" National Institute for Physics and Nuclear Engineering, 30 Reactorului Street, RO-077125, Bucharest-Magurele, Romania

[2]FRM II and Physik Department E21, Technische Universität München, 85747 Garching, Germany

[3]National Institute of Materials Physics, 105 Atomistilor Street, RO-077125 Bucharest-Magurele, Romania

[*]Corresponding author *Email:* nikolay.djourelov@eli-np.ro

Abstract. We propose to obtain an intense beam of moderated positrons (e_s^+) with an intensity of the primary positron beam of 1×10^6 - 2×10^6 $e_s^+ s^{-1}$ by the (γ, e^+e^-) reaction using an intense γ-beam of 2.4×10^{10} $\gamma\, s^{-1}$ with energies up to 3.5 MeV. Using fully circularly polarized γ-beam we aim to obtain an intense, polarized positron beam with a polarization degree of 31-45%. Higher degree of polarization would also be possible with reduced beam intensity. The beam will be transported to different detector systems through beam lines, via solenoidal magnetic fields. Polarized positron beams open up a totally unexplored research area in applied physics studies of Fermi-surfaces, defects, interfaces *etc.*, where polarized electrons can be studied. A simple, fast scintillator detector system for γ-induced positron annihilation lifetime spectroscopy for studies of bulk samples is proposed. The ELI-NP facility will be user-dedicated and unique for positron research in the Eastern Europe. It will provide a simple source setup, with easy access for upgrades of the converter/moderator assembly toward more sophisticated setups, providing a more intense and brighter positron beam. The beam will have the world highest intensity of polarized positrons for material science studies and, therefore, it will become a unique tool for the investigation of magnetic samples.

Key words: gamma beam, positron production, slow positrons, polarized positrons.

1. INTRODUCTION

The positron [1, 2] is for many years a well-established probe for defect spectroscopy and offers the possibility of defects examination in metals, semiconductors and isolators [3]. The energetic e^+ from an isotope source as a probe scans the specimen over a wide range of up to several 100 µm depth, depending on the material density. Many defect types, for instant open-volume like defects and negatively charged impurities, have an attractive potential for e^+ and trap them very efficiently. The high trapping efficiency and the long diffusion length are responsible

for the enormous defect sensitivity of e^+. As important as the sensitivity is that the state of the e^+ depends on the electronic structure of the specimen. Since the properties of the annihilation radiation vary with the state of the e^+, details of the electronic structure get observable by detecting this radiation. By measuring the positron lifetime (PALS) the defect types and their concentration can be revealed. The deviation from the collinearity of the radiation and the broadness of the annihilation line provides information about the momentum distribution of the electrons in the specimen. This measurements are the scope of the angular correlation of the annihilation radiation (ACAR) method and of the Doppler broadening spectroscopy (DBS). Another technique called aged momentum correlation (AMOC) combines PALS and DBS and records time-correlated energy spectra and it is useful in studies of reactions involving positrons [4].

These techniques have been performed successfully for decades with the help of radioactive e^+ emitters and still provide an important contribution to the exploration of defects and the electronic structure of various systems. The range of applications can be enlarged enormously if a mono-energetic e^+-beam is used for the experiments. Due to its tunable energy, depth resolved measurements can be performed.

Positronium (Ps), the bound state of a e^+ and an e^-, is a sensitive and unique probe for studies of nano-porous materials. In pores with a size larger than about 0.7 nm, Ps atoms can be formed. The very long lifetime of *ortho*-Ps (up to 142 ns) and the relatively narrow momentum distribution of *para*-Ps provide sensitive detection tools of the dimensions of nano-scale pores. Moreover, they are indispensable and very sensitive tools to monitor the connectivity of pore networks and the open or closed porosity. A unique feature is the possibility to quantify pore size distribution, including of the pores which are not connected to the exterior of the sample and which are not visible by standard adsorption-desorption isotherm (BET) techniques.

Positron annihilation techniques, being non-destructive, allowing depth profiling down to a few micrometers and detection of open-volume defects (vacancies, dislocations *etc.*) at single ppm concentrations, constitute a valuable and complementary method, compared to other solid-state-physics analysis methods [5].

In surface science, positron annihilation-initiated Auger electron spectroscopy (PAES) have been proven to be an extremely surface sensitive technique, allowing one to detect the Auger electrons emitted only from the topmost surface layer.

Also, coincident Doppler broadening spectroscopy (CDBS) enables one to extract the momenta of core electrons and therefore to extract chemical information on the same quality as from X-ray photoelectron spectroscopy (XPS), but with bulk sensitivity. Angular correlation of annihilation radiation (ACAR) has been proven to be a useful method to determine bulk band structure of crystalline materials, including nano-crystallites embedded in a host matrix; again, this technique is opposed to conventional angle-resolved ultraviolet photoelectron spectroscopy,

which is a surface technique, *i.e.*, its sensitivity is limited to few layers from the sample surface.

Consequently, positron annihilation-induced techniques may be either extremely surface sensitive, or bulk sensitive, by providing information on the same quality as conventional analysis methods (UV or X-ray photoelectron spectroscopy).

The first part of every beam of slow/moderated e^+ (e_s^+) beam is the source which, in the case of a small laboratory beam systems, is usually a radioactive isotope. From the various existent β^+ sources, ^{22}Na, ^{58}Co and ^{64}Cu are mainly used for the beam production.

With a typical setup, like the slow positron laboratory beam at the Technical University in Munich [6] using a ^{22}Na source of 6 mCi, it is possible to create a beam with up to 2×10^4 e_s^+ s^{-1}. At the same laboratory a e^+-beam with an intensity of 2×10^5 e_s^+ s^{-1} was attained by using a self-made ^{64}Cu source. If a solid Neon moderator (instead of a tungsten one) and a stronger source (*e.g.*, ^{58}Co) are used, higher intensity of ~ 10^6 e_s^+ s^{-1} is achievable.

In order to create beams with even higher intensities, another kind of source has to be utilized, based, for example, on the mechanism of pair production [7]. Using a brilliant γ-beam, e^+e^- pairs can be produced in a suitable target by pair production. A well-designed positron source would hence allow to create a e_s^+-beam of high intensity. In addition, the brightness can be further enhanced by e_s^+ re-moderation.

There are two fundamentally different setups for the creation of a e_s^+-beam using a brilliant γ-beam. Either the γ-to-e^+ converter and the moderator are separate components, or the converter is used as e^+ moderator as well, and hence the e_s^+ are extracted directly from the converter surface. The production and subsequent moderation in the same component is called self-moderation. In order to create a bright e^+-beam, a moderator should be used with high efficiency and should provide a narrow band width of the emitted e^+. However, the choice of the applied moderator material strongly depends on the final source layout.

The γ conversion into e^+e^- pairs takes place in a material with high nuclear charge Z, such as Pt or W (also suitable moderator materials), since the pair production cross-section σ_{PP} increases approximately proportional to Z^2. At a γ energy of 2.5 MeV, the pair production cross-section σ_{PP} for Pt and W amounts to 2.386 and 2.713 barn/atom, respectively. In addition, the converter material should have a high melting temperature due to the high local heat dissipation. Suited materials for e^+ moderation are metals with negative positron work function Φ^+ such as Pt (Φ^+= −1.95 eV) and W (Φ^+= −3.0 eV) or solid rare gases.

In general, the key features of a low-energy e^+-beam produced using a high-brilliant γ-beam would be the following:

– γ energy: the energy of the γ-beam can be varied in the range of several MeV in order to maximize the e^+ production and emission rate, and the yield of e_s^+, as well.

– Energy cut: due to the possibility to use a collimator, which acts as a low energy cut, unwanted γ-rays are produced with energy less than $2m_0c^2$ which do not contribute to the pair production. Therefore, the heat load compared to LINAC or reactor based e^+ sources is expected to be considerably lower.

– Polarization: using a switchable fully circularly polarized γ-beam, a spin-polarized e^+-beam can be created. Omori *et al.* have experimentally proven the efficient propagation of polarization from laser photons through Compton scattering on electron beam to the created gamma-beam and then by pair production to positrons [8]. Since the e^+ spin polarization is almost entirely maintained during moderation, spin-dependent experiments may become feasible.

– Access: The source area of the γ-beam will be easily accessible. This would facilitate the change of the source setup considerably and opens the door for novel converter and moderator setups regarding sophisticated geometries and new materials.

– Radiation field: due to the well-defined, relatively low energy of the γ-beam, of maximum 3.5 MeV, the creation of radiation induced defects is expected to be lower than that at e^+ source setups using bremsstrahlung targets at LINACs or γ-rays produced at nuclear reactors. In addition, no radioactivity is created by activation [9].

2. PHYSICS CASES

2.1 SLOW POSITRON BEAM PRODUCTION BY GAMMA-RAY BEAM

2.1.1. Gamma-ray beam characteristics

Fig. 1 – Time structure of the γ-beam. The macro bunches are provided with a repetition of 100 Hz, and each macro bunch will consists of 32 micro bunches of 1 ps, separated by 16 ns.

The γ-beam time structure is illustrated in Fig. 1. The macro bunches are provided with a repetition of 100 Hz, and each macro bunch will consists of 32 micro

bunches of approximately 1 ps, separated by 16 ns. The data concerning the γ-beam energy and divergence characteristics are provided by EuroGammas [10] and describe the space position coordinates, energy and momentum direction vector of each γ-ray in a microbunch at the moment of the Compton-collision for γ-ray production. It has been demonstrated by EuroGammas that the provided data meet the γ-beam specifications summary of a collimated γ-beam with narrow bandwidth (less than 5.0×10^{-3}) [11]. However, due to the fact that we need to use wide bandwidth γ-beam (1.022-3.5 MeV) we cannot refer to the narrow bandwidth specifications.

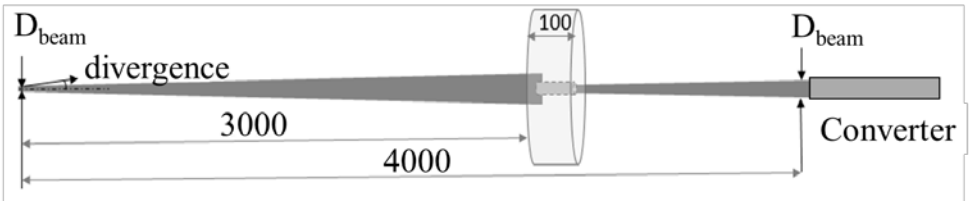

Fig. 2 – Scheme for GEANT4 simulation of the γ-beam energy cut by a tungsten collimator. The sizes are in mm.

The interaction chamber for e^+ production can be placed at a distance of 4 m from the interaction point where low energy γ-rays will be created (as discussed in details in Section 3). We have used GEANT4 simulation to crosscheck the effect of azimuthal angle cut on the energy spectrum and the γ-beam dimensions of the γ-to-e_s^+ converter. The scheme is plotted in Fig. 2.

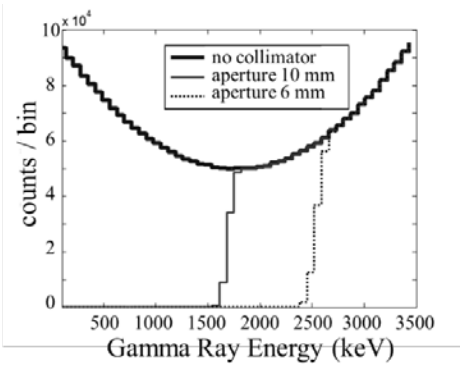

Fig. 3 – Energy spectra of γ-rays as described in Fig. 2.

The application of different collimator aperture is almost entirely analogical to azimuthal angle cut and the effect on energy spectrum is well seen in Fig. 3. The cut

effect on the beam size can be followed in Fig. 4 where the intensity profile of γ-beam at the interaction point with the converter, without collimator and with collimator aperture of 6 mm, are presented. It is obvious that the low energy γ-rays are predominantly distributed in peripheral area of the beam profile. Due to the fact that γ-rays with energy less than $2m_0c^2$ do not contribute to pair production, an aperture of 12 mm was found to be most suitable. At this aperture 41% of the initial γ-beam intensity is cut. What is extremely important is that the FWHM, at the position of interaction with the converter, of the γ-beam intensity profile is D_γ~ 6.5 mm and it is almost not affected by the collimator aperture down to 6 mm. Further decrease in FWHM can be achieved by smaller aperture but at the expense of significant loss of intensity.

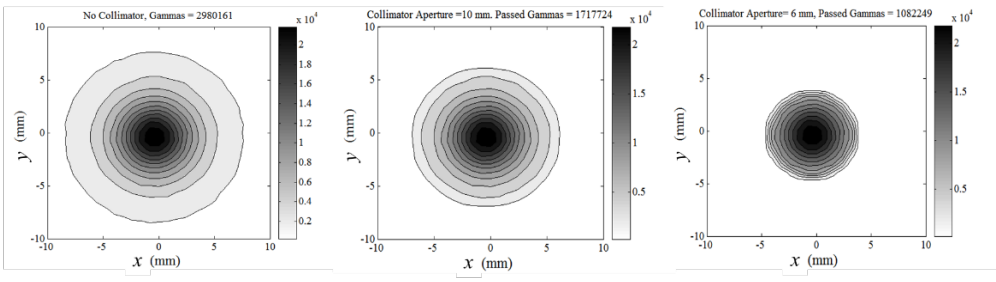

Fig. 4 – Intensity profile of γ-beam at the interaction point with the converter without collimator (left) and after collimation at selected apertures, 10 mm (middle) and 6 mm (right).

2.1.2. Electron-positron pair production

When a γ-quantum with an energy E_γ enters a solid with an atomic number Z it loses energy mainly due to three processes: the photoelectric effect (PH), the Compton scattering (CS), and the pair production (PP) process. The cross-sections are as follows [7]:

$\sigma_{\mathrm{PH}} \propto Z^n/E_\gamma^m$ - n, m within 3 and 5

$\sigma_{\mathrm{CS}} \propto 1/E_\gamma$

$\sigma_{\mathrm{PP}} \propto Z^2 f\left(E_\gamma, Z\right)$ - the Z dependence is dominated by the Z^2 term and $f\left(E_\gamma, Z\right)$ increases continuously with energy.

The pair production in a solid occurs in the electric field of a nucleus or of an electron, with a much lower probability in the latter case. Due to the energy conservation, there is a threshold for pair production, which equals the rest masses of the e^- and of the e^+, as well as a certain amount which is transferred by the recoil

to the field generating nucleus or electrons. For the pair production in the vicinity of a nucleus this amount is negligible, but in the case of an electron the threshold is doubled to four electrons rest masses.

There are basically three concepts of e^+ sources, utilizing pair production, which differ only in the method on how the high energy γ-quanta are produced. The first concept uses high energy electrons created by a LINAC, which are dumped onto a high-Z target in order to create high energy bremsstrahlung [12, 13]. The second, which is implemented at the research reactor in Delft, The Netherlands, uses the high flux of radiation which originates from the fission process at the core of a nuclear reactor [14]. The third is also a reactor based concept, but in contrast to the Delft concept, the high flux of thermal neutrons is used to generate high energy γ-quanta by the nuclear reaction ^{113}Cd (n,γ) ^{114}Cd. The world's strongest e^+ source NEPOMUC (NEutron induced POsitron source MUniCh), at the Heinz Maier-Leibnitz (FRM II) research reactor near Münich, Germany, uses this method and generates up to 1.1×10^9 e_s^+ s^{-1} [15].

2.1.3. Positron moderation

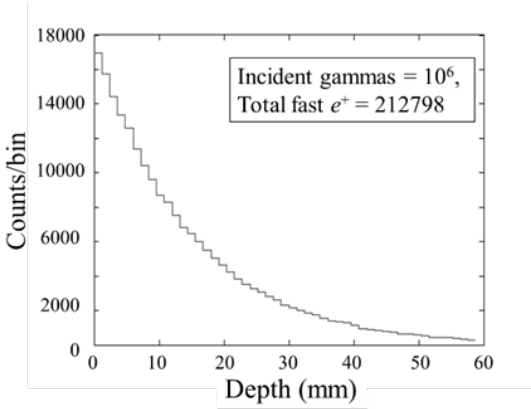

Fig. 5 – Depth profile of created fast e^+ by a 2.5-MeV γ-beam with energy distribution of 0.5 MeV (FWHM) interacting with a tungsten target. The total number of created fast e^+ is approximately 21% of the incident γ-rays.

In the first steps we used GEANT4 to model the fast e^+ production for the γ-to-e^+ converter at Extreme Light Infrastructure Nuclear Physics (ELI-NP). GEANT4 is a free software package composed of tools which can be used to accurately simulate the passage of particles through matter. Using this simulation program the number of e^+ and electrons emitted from a target can be calculated. The pair-production efficiency was simulated by pointing a 2.5-MeV γ-beam with energy distribution of 0.5 MeV (FWHM) to a tungsten target with large dimensions in order

to absorb the γ-beam. At the moment of a pair production the e^+ depth and energy were recorded. The result plotted in Fig. 5 shows the depth position of created e^+ in case of a W target. It can be seen that, due to the high γ-beam energy, 6 cm of bulk material are needed to absorb 99% of the γ-rays.

The effect of the fast e^+ absorption by the surrounding material can be seen in a simulation where a narrow γ-beam is shot into a W rod (see Fig. 7). With the decrease of the rod radius the fraction of created fast e^+ which escapes the rod increases. In the ideal case of an infinitely narrow γ-beam and rod this fraction will reach 21% - the efficiency for W to convert 2.5-MeV γ-rays to fast e^+ in the bulk. In order to moderate fast e^+ good surface to volume ratio is needed. The conclusion comes naturally that for efficient production of e_s^+ a layered structure along γ-beam direction, as shown in Fig. 8, has to be used.

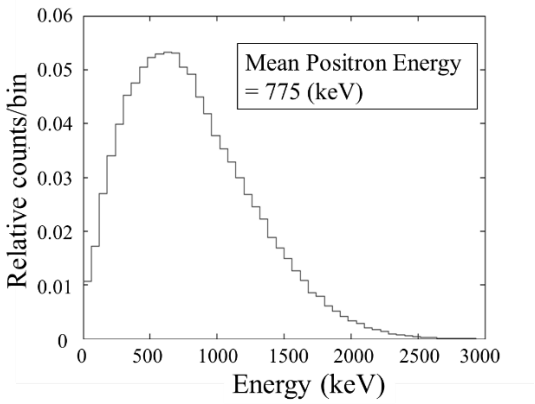

Fig. 6 – Energy spectrum of created fast e^+ by a 2.5-MeV γ-beam with energy distribution of 0.5 MeV (FWHM) interacting with a tungsten target. The average energy is 775 keV.

Unfortunately, GEANT4 does not support simulation of physics processes for energies bellow 50 eV and, therefore, it cannot be used directly for simulation of e^+ moderation. In order to describe the moderation of fast e^+ we have developed a user physics process and implemented it in GEANT4. This process can be shortly described by the following steps: we track the created positrons in the moderator and when the e^+ energy (E_+) is below 25 meV (thermalized) we find the distance d to the nearest surface, and calculate the probability $p = \exp\left(-d/L_+\right)$ for a thermalized e^+ to diffuse to the surface and, finally, with probability $b \times p$ a new particle (moderated e^+) is created out, but very close to the moderator surface, and emitted normal to the surface with energy $\varepsilon_+ = \left|\Phi^+\right|$. The coefficient $b = 0.4$ is the branching ratio, and $L_+ = 135$ nm is the e^+ diffusion length for W. The geometry for the W-foil moderator and the e^+ source described in [16] in transmission and in [17] for reflection mode

was reproduced; moderation efficiency obtained by GEANT4 simulation was 6.1×10^{-4} (transmission mode) and 2.8×10^{-3} (reflection mode), respectively, values which are in satisfactory agreement with the experimental ones of 4×10^{-4} and 3.8×10^{-3}, respectively. Additional validation was done by simulation of the two converters with simple geometries for high intensity (HI, see Fig. 8) and high-brilliance (HB) e^+ source proposed for ELI-NP by Hugenschmidt *et al.* [9]. The corresponding conversion efficiencies estimated by Hugenschmidt *et al.* are 3×10^{-4} and 8.5×10^{-8} and these values are in good agreement with 2×10^{-4} and 1×10^{-7}, respectively, as obtained by GEANT4. Consequently the user defined physics of the e^+ moderation works well and one can apply it for complex geometries in order to optimize the size parameters.

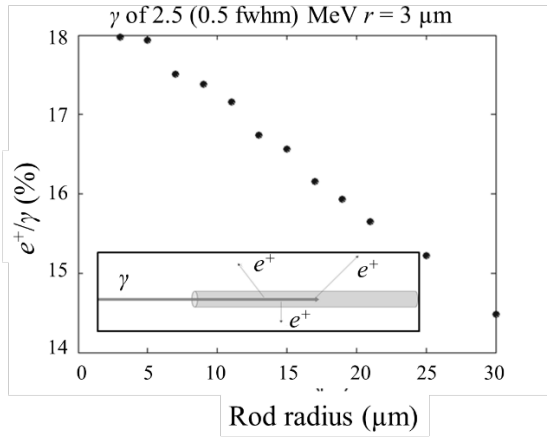

Fig. 7 – Yield of escaped fast e^+ as a function of the rod radius. The γ-beam is with energy of 2.5 MeV (FWHM = 0.5 MeV) and radius $r = 3$ μm.

It has to be mentioned that the proposal for HI and HB converters and the efficiency estimations of Hugenschmidt *et al.* are valid for micron size γ-beams, which is not the case of the current status of ELI-NP project (see the end of Section 2.1.1).

The target geometry which we propose is shown in Fig. 9. Actually the design is very close to what was presented in Fig. 8, but with bottom and side walls. It is known as venetian blind geometry, which is open in the direction of the slow positron extraction. The idea is that these walls will interact with fast e^+ which escape from the transversal walls and part of them will be moderated in reflection mode. There are two restrictions on the geometry parameters. The length is fixed to $L = 30$ cm, and the aspect ratio H:G of the gaps is fixed to AR = 3:1. The reason we have chosen these values is explained in the next two sections. The optimization of the geometry parameters in order to obtain the best γ-to-e_s^+ conversion efficiency can be done

directly with GEANT4 simulation developed by us. However, a run for one set of parameters with 3×10^6 γ in the run takes about 4 hours to be completed, and the fact that we have to optimize both d and H, we needed a quicker way to find good initial parameters. Therefore we have developed a way to first estimate roughly the best parameters to be used as initial values for subsequent optimization by GEANT4 simulations.

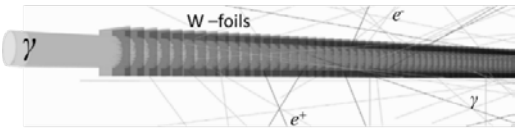

Fig. 8 – Sketch of the interaction of a 200 μm wide γ-beam with a target consisting of 2500 W foils (300×300×10 μm^3) in sequence, separated by gaps of 50 μm.

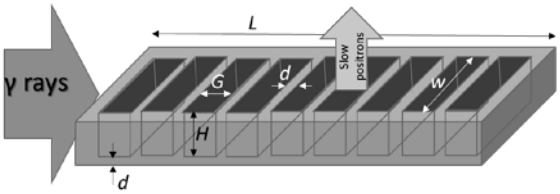

Fig. 9 – Geometry (venetian blind) of the proposed converter made of tungsten.

The γ-to-e_s^+ conversion efficiency Γ which is a function of the H, G, d, w, n, D_γ parameters can be split into few parts:

$$\Gamma\left(H, G, d, w, n, D_\gamma\right) = \Gamma_{\mathrm{CS}}\left(H, w, D_\gamma\right)\, \Gamma_{\mathrm{abso}}(d, n)\, \Gamma_{\mathrm{th}}(d)\, \Gamma_{\mathrm{a}}(H, G, w), \qquad (1)$$

where $n = L/(G + d)$ is the number of transversal foils, $\Gamma_{\mathrm{CS}}\left(H, w, D_\gamma\right)$ is the cross-section of the front side of the converter (a rectangle with sizes H, w), with the γ-beam profile represented for simplicity with a Gaussian having FWHM $D_\gamma = 6.5$ mm, $\Gamma_{\mathrm{abso}}(d, n) = 1 - \exp(-nd/\mu)$ is the γ-rays stopping profile (see Fig. 5), $\Gamma_{\mathrm{th}}(d)$ is the efficiency of fast e^+ to be moderated in a stack of big number of large foils with thickness d, and $\Gamma_{\mathrm{a}}(H, G, w)$ is the probability that a fast e^+ emitted from the walls is caught by the converter (see Eq. 2).

$$\Gamma_{\mathrm{a}}(H, G, w) = (2\pi - \mathrm{atan}(w/2H))(2\pi - \mathrm{atan}(G/2H)) \qquad (2)$$

The parameters G and n are calculated from the others. The parameter w was initially fixed to 16 mm, while D_γ = 6.5 mm is known. The efficiency $\Gamma_{CS}\left(H, w, D_\gamma\right)$ is then calculated (see Fig. 10).

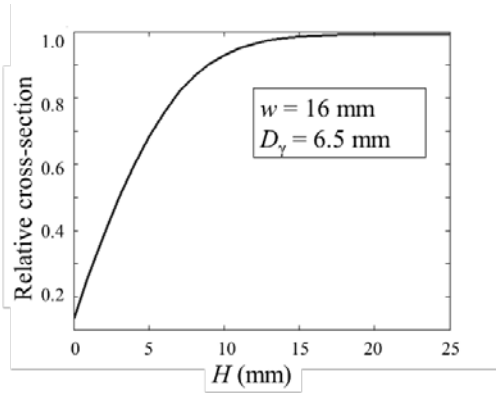

Fig. 10 – Relative cross-section of a transversal rectangle converter foil with sizes H and w, with a Gaussian shape profile with FWHM D_γ = 6.5 mm, with longitudinal axis of symmetry.

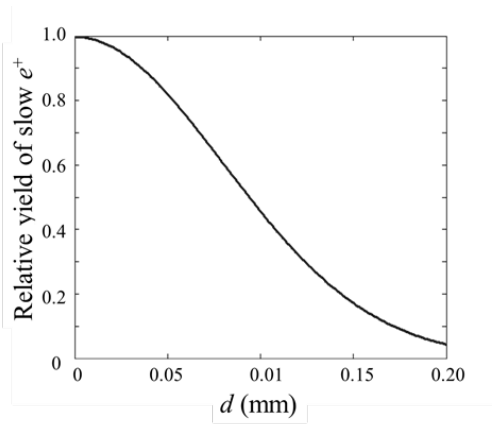

Fig. 11 – Relative yield of e_s^+ as function of the thickness of tungsten foil as simulated by GEANT4 for a stack of large foils irradiated by gamma rays with characteristics given in Section 2.1.1.

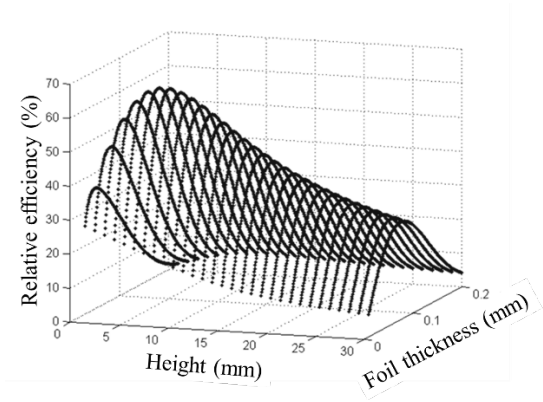

Fig. 12 – Relative efficiency $\Gamma\left(H, G = \frac{H}{3}, d, w = 16\text{ mm}, n = \frac{L}{H+d}, D_\gamma = 6.5\text{ mm}\right)$ as a function of the foil thickness, *d*, and the gap height, *H*.

The result for $\Gamma\left(H, G = \frac{H}{3}, d, w = 16\text{ mm}, n = \frac{L}{H+d}, D_\gamma = 6.5\text{ mm}\right)$ is plotted in Fig. 12. The best efficiency is obtained at H = 6 mm and d = 0.060 mm. We have also checked the influence of the gap width, *w*, on the relative efficiency, but we found that it has small impact when was chosen to be about double D_γ. These values were used for GEANT4 simulations to refine the optimization. The results are summarized in Table 1. The results show that the best absolute efficiency is $\Gamma_{\text{best}} = 8.2\times10^{-5}$ obtained at foil thickness d = 80 μm and gap height of H = 6 mm.

Table 1

Absolute γ-to-e_s^+ conversion efficiency $\Gamma\left(H, G = \frac{H}{3}, d, w = 16\text{ mm}, n = \frac{L}{H+d}, D_\gamma = 6.5\text{ mm}\right)$ for the γ-rays described in Section 2.1.1 as simulated by GEANT4.

H (mm) \ *d* (mm)	5	6	7	8
0.06	7.4×10^{-5}	7.6×10^{-5}	7.5×10^{-5}	7.3×10^{-5}
0.07	7.5×10^{-5}	7.7×10^{-5}	7.6×10^{-5}	7.5×10^{-5}
0.08	7.8×10^{-5}	8.2×10^{-5}	8.1×10^{-5}	7.6×10^{-5}
0.09	7.4×10^{-5}	7.4×10^{-5}	7.2×10^{-5}	7.0×10^{-5}

One of the critical points in the converter design is the extraction of e_s^+. Problems appear due to the short distances between the converter elements and, consequently, of the screening of the electric field applied for extraction of e_s^+. Simulations with COMSOL [18] were performed. Slow positrons are emitted normal to the surface of the foils face, uniformly distributed on it, with an initial energy of $\varepsilon_+ = 3$ eV. For more realistic simulation we have implemented in COMSOL the feature that low energy e^+ can be reflected from tungsten surfaces with a probability

of 0.6 otherwise they annihilate [19]. In Fig. 13 the potential difference between the electrode and an extraction mesh is set to 60 V. The magnitude of this potential difference has to be kept low in order to avoid large energy spread of the extracted e_s^+. It is seen that about 40% of the e_s^+ are extracted, due to lack of electric field gradient in the direction towards the extraction grid. In case (a) where the converter is attached to the electrode at U = 60 V and the extraction mesh is at ground, the e_s^+ emitted from the lower part of the transversal foils simply impinges the facing foil and annihilate there, while in the case (b) where the converter is at floating potential between the electrode and the extraction mesh, the slow positrons from the same part of the foils are subjected to electric field gradient pushing them back to the foil (that is why they cannot be extracted).

2.1.4. Extraction of moderated positrons

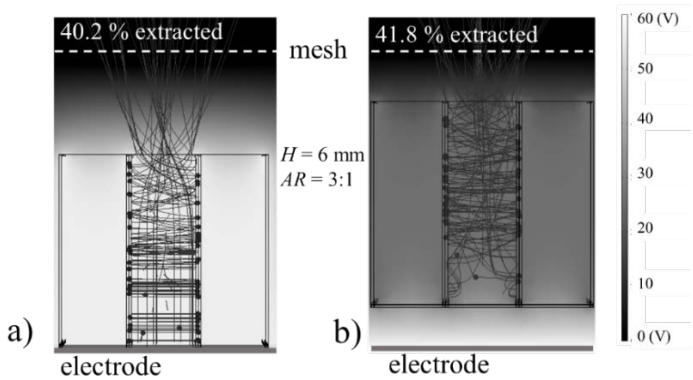

Fig. 13 – COMSOL simulations of e_s^+ trajectories in a converter cell with extraction mesh at ground (a) the converter is attached to electrode at 60 V, and (b) the converter is at floating potential between the electrode and the extraction mesh. The distance between the electrode and the mesh is 9 mm in both cases.

The three basic ways to achieve some electric field gradient in order to extract e_s^+ towards the extraction mesh is to decrease the aspect ratio, to make segmentation of the transversal foils, or to increase the voltage. At a fixed aspect ratio the combination of some segmentation with voltage increase is not advisable because it leads to large energy spread of extracted e_s^+.

In Fig. 14 the extraction efficiency as a function of the applied potential difference between the extraction mesh and the electrode for non-segmented converter with H = 6 mm and AR = 3:1 is plotted. It can be seen that high potential is needed for successful extraction. The performance of the geometry (b) (see Fig. 13), where the converter is at floating potential, at low potential difference, is slightly better than the geometry (a) but reaches saturation at lower level of

extraction efficiency. Another very important characteristics of the extracted e_s^+ is the energy spread shown in Fig. 15. This information has to be taken into account together with divergence for the subsequent beam formation.

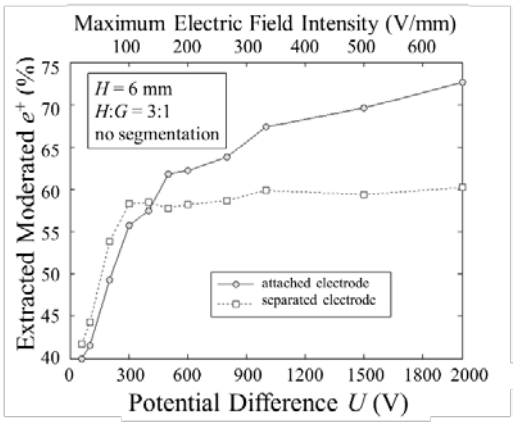

Fig. 14 – The fraction of extracted e_s^+ as a function of the applied potential difference between the electrode and the extraction mesh placed at 9 mm from the electrode for the two geometry cases shown in Fig. 13.

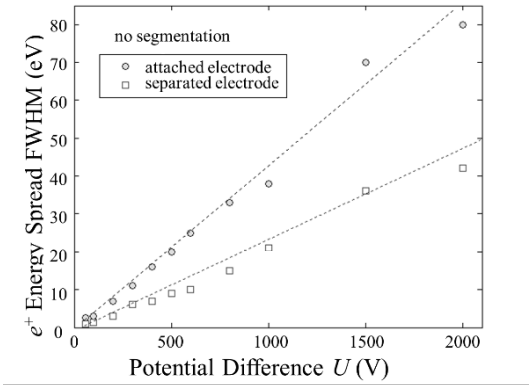

Fig. 15 – The energy spread of extracted e_s^+ as a function of the applied potential difference between the electrode and the extraction mesh placed at 9 mm from the electrode for the two geometry cases shown in Fig. 13.

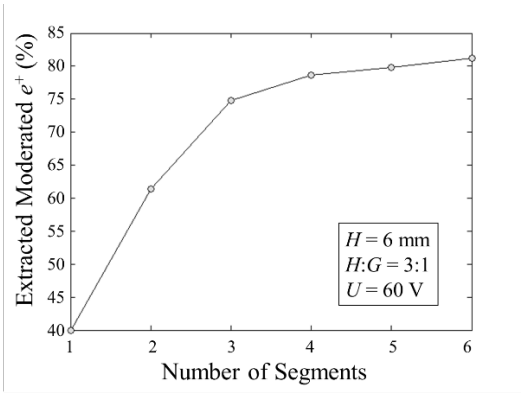

Fig. 16 – The fraction of extracted e_s^+ as a function of the number of segments for converter with aspect ratio AR = 3:1 and H = 6 mm, and potential difference between the electrode and the extraction mesh of U = 60 V. The extraction mesh is at 9 mm from the electrode.

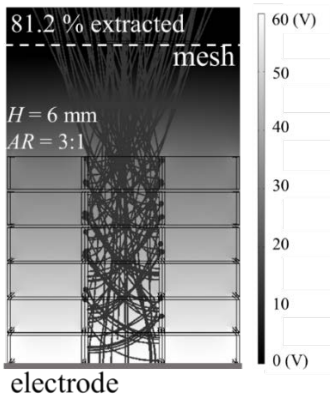

Fig. 17 – Electric potential map for a converter segmented into 6 layers; converter aspect ratio AR = 3:1, H = 6 mm, and U = 60 V. The electrode-mesh distance is 9 mm. Segment 1 is attached to the electrode, while segments 2 to 6 (electrically insulated from each other) are at floating potential.

The effect of segmentation is plotted in Fig. 16 for a segmented converter with H = 6 mm, AR = 3:1, and U = 60 V. A map of the electric field potentials for a converter segmented into 6 layers is given in Fig. 17. The segmentation effect on the creation of electric field gradient to extract e_s^+ towards the extraction mesh is clearly seen. The method of segmentation is very effective achieving more than twice extraction efficiency (81.2%, for 6 segments, and U = 60 V) as compared to the non-segmented converter.

Due to the fact that the aspect ratio influences the extraction and production efficiencies in opposite ways a compromise is necessary to be found. As seen in Fig. 18 for non-segmented converter of length of L = 30 cm and H = 6 mm such a compromise is an aspect ratio in the range from 2 to 3.

With a large number of segmentations close to "ideal" electric field gradient can be achieved. In this case it is easy to calculate the aspect ratio condition at which the e_s^+ will have minimum interactions with walls. Moderated positron emitted from the middle of a transversal foil can be taken as a representative. This e_s^+ will travel following a longitudinal path G for a time $t = G/\sqrt{2e\varepsilon_+/m_e}$, while in transversal direction it is subjected to electrical field acceleration, so for the time t it will transversally move by $h = eUt^2/(mH)$. The condition to escape from the gap without interaction with walls is $h > H$. Finally, we come to the conclusion that the aspect ratio has to be kept at $AR < \sqrt{U/(2\varepsilon_+)} = 3.15$, for U = 60 V.

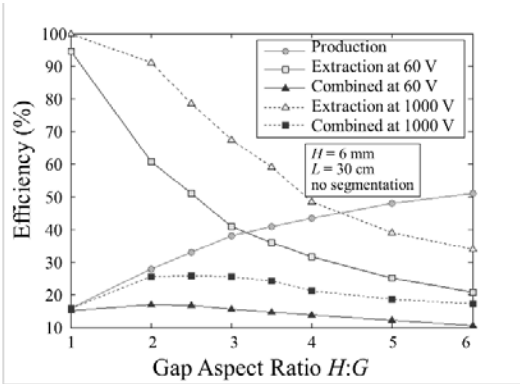

Fig. 18 – The e_s^+ production efficiency and the e_s^+ extraction efficiency as a function of the aspect ratio H:G for H = 6 mm for two potential differences of U = 60 V and 1000 V between the electrode attached to the converter and the extraction mesh placed at 9 mm from the electrode.

Additionally we have studied the effect of the strength of a uniform magnetic field with magnetic induction vector (0, 0, B_z) along the direction of extraction of the e_s^+. The usefulness of this magnetic field is that it will force e_s^+ to make precession around the magnetic field vector, so, they can survive longer between the two facing each other transversal walls of a cell of the converter which will give them time to be accelerated by the electric field of the extraction mesh. However, these e_s^+ which are emitted from the side walls of the converter will survive shorter. In case of strong magnetic field the e_s^+ will be forced to return back to the surface. These effects are schematically presented in Fig. 19. A proper tuning of the magnetic field strength is necessary to optimize the extraction of the e_s^+. It was performed with COMSOL for

a non-segmented and segmented into four layers converter. The results are plotted in Fig. 20 and show that the extraction efficiency can be improved by proper choice of the magnetic field intensity.

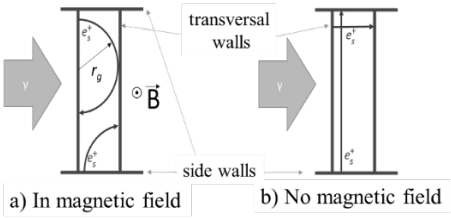

Fig. 19 – Examples of trajectories of e_s^+ emitted from the side and transversal walls of a cell of the converter (a) in magnetic field and (b) without magnetic field. The point of view is against the direction of extraction of the e_s^+.

The conclusion from the current section is that by the help of segmentation and proper choice of electric potential and magnetic field strength we can extract almost all of the e_s^+. However, attention has to be paid on consequences affecting the beam formation (focusing) (see the discussion in Section 3.4).

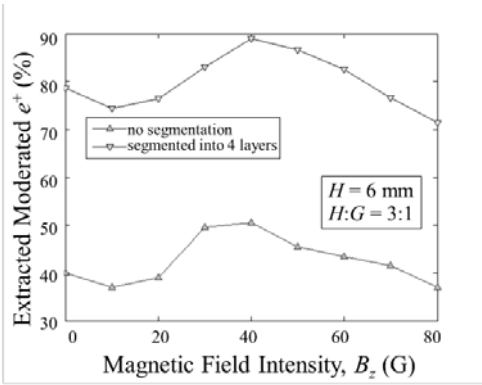

Fig. 20 – Fraction of extracted of e_s^+ from a converter in uniform magnetic field with magnetic field vector along the direction of the extraction, simulated by COMSOL. The cases are for non-segmented and segmented into four layers converter, AR = 3:1, U = 60 V.

2.1.5. Converter design to work in parasitic mode

As it was described in Section 2.1.1, an important feature of the γ-beam is the correlation between the energy and the scattered angle of the γ-rays, the higher the energy the smaller the angle [10]. This allows not only to filter out the low energy γ-rays with a collimator, as demonstrated by simulations (see Fig. 2) but, also, if

central holes are drilled in the transversal foils of the CMA (see the scheme in Fig. 21), fraction of the high energy rays can be transmitted without interaction. If the holes diameter is greater than 2.5 mm then the intensity of the 3.5 MeV will not be affected, as can be seen from GEANT4 simulation results shown in Fig. 22. This will allow to use the positron source at ELI-NP in parasitic mode (as recommended by The ELI-NP International Scientific Advisory Board Meeting, 18-19 June 2015, Romania), *i.e.*, simultaneously with nuclear physics experiments because the last require only narrow bandwidth γ-beam. The performed simulations for γ-to-e_s^+ conversion efficiency by GEANT4 showed also that the holes (2.5 mm) option of the CMA will reduce the e_s^+ intensity to 82%.

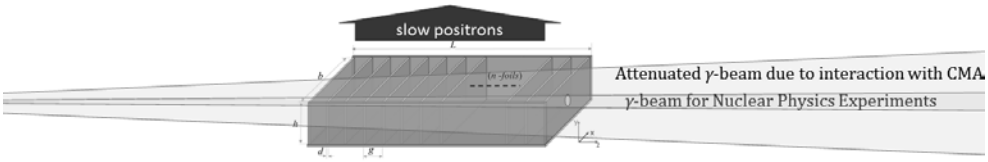

Fig. 21 – Converter/Moderator assembly with holes in the transversal foils.

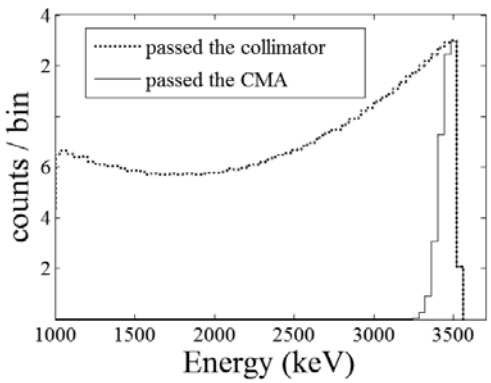

Fig. 22 – Energy spectra of the γ-rays which passes the collimator for elimination of γ-rays not producing e^+-e^- pairs, and of the γ-rays which passes through the holes of 2.5 mm in diameter in the CMA transversal foils.

2.2 DEPTH PROFILING WITH MONOENERGETIC POSITRONS

Beam of monoenergetic e_s^+ with variable energy can be used as a e^+ source and combined to the different positron annihilation techniques. Stopping profile of

monoenergetic e^+ of initial kinetic energy E_+ in matter, $P(z, E_+)$, is described as the Makhov's distribution,

$$P\left(z, E_+\right) = \frac{mz^{m-1}}{z_0^m}\exp(-(z/z_0)^m), \text{ where } z_0 = \frac{AE_+^r}{\rho\Upsilon(1+1/m)} \quad (3)$$

In these formula, E_+ is the initial kinetic energy of e^+, in keV, ρ denotes the mass density of the sample in g/cm^2, Υ is the gamma function, while $r = 1.6$, $m = 2$ and $A = 4.0$ μg cm^{-2} keV^{-r} are empirical parameters [3]. The average penetration depth is $\bar{z} = AE_+^r/\rho$, and the distribution width is proportional to z_0.

The depth resolution power of monoenergetic e^+ is illustrated by Makhov's profiles (Eq. 3) in Cu, plotted for several E_+ in Fig. 23. It can be seen from the figure that depth resolution power attains about 10 nm at energies below 1 keV and, despite of an appreciable increase in width, remains still reasonable up to about $E_+ \approx 30$ keV, corresponding to penetration depths approaching 1 μm.

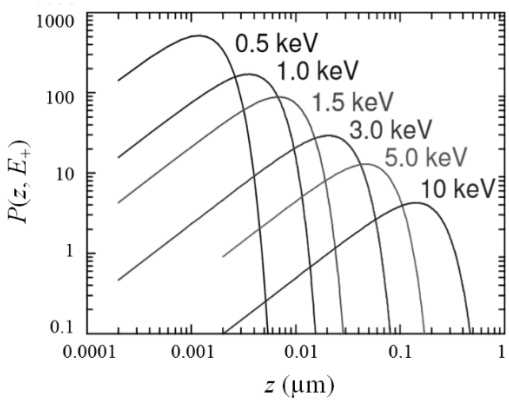

Fig. 23 – Implantation profiles of monoenergetic e^+ in Cu. Energy values are inserted in the figure.

2.3 POLARIZED POSITRONS

Polarization of e_s^+ was discovered by Zitzewitz *et al.* in 1979 [20]. Few years later van House *et al.* [21] have studied e^+ moderation process with ^{22}Na source (very strong source of 100 mCi) based e^+-beam, with electrostatic guidance and a degree of polarization $P = (48 \pm 2)\%$ and intensity of 5×10^5 e_s^+s^{-1}. They have shown that with absorber it is possible to achieve a degree of polarization as high as $P = (69 \pm 4)\%$, with reduced intensity. Maekawa *et al.* [22] built a similar e^+-beam, but using a ^{68}Ge–^{68}Ga e^+ source produced from the ^{69}Ga(p,2n)^{68}Ge nuclear reaction by irradiating a GaN substrate with 20 MeV protons for 400 h in 20 cyclotron sessions. The degree of spin polarization of the e^+-beam was determined as

(47 ± 8)% from the magnetic field dependence of the *p*-Ps intensity in fused silica, while the achieved beam intensity was 5×10^3 $e_s^+ s^{-1}$.

A few other methods to produce polarized e^+ are being considered by the linear collider community. The concept is to use e^+e^- pairs created by converting circularly polarized γ-rays. The circularly polarized γ-rays may come from one of these processes: helical undulator radiation by unpolarized electron beams [23], Compton scattering of circularly polarized laser-light off a high-energy electron beam [24,8] (a process that will be used also within the ELI-NP project), and Bremsstrahlung of longitudinally polarized electrons in high-*Z* amorphous targets [25].

The production of highly polarized short-pulse positrons has been demonstrated experimentally for the first time at KEK, Japan [8]. Using a circularly polarized laser beam of 532 nm scattered off a high-quality, 1.28 GeV electron beam, the authors have obtained polarized positrons with an intensity of 2×10^4 e^+ per bunch and the degree of positron polarization has been determined to be 73 ± 15 (stat) $\pm$ 19 (syst)% by means of a newly designed positron polarimeter. Omori *et al.* also reported a very good agreement of the experimentally determined degree of spin polarization with the value of 77% as obtained by GEANT4 simulations of the experiment [8].

Spin-polarized e^+ provide a new, atomic-scale view on the magnetism and electronic structure of magnetic materials. Its kinetic energy can easily be tuned, enabling depth-profiling studies of a large variety of sub-micron thin films.

The influence of slowly varying electric and magnetic fields on polarized electron beams is described in [26]. Few cases are described which for non-relativistic beam can be summarized as follows: a) Deflecting low energy electrons by electric field over an angle of $\pi/2$ change the longitudinal polarization to transversal (or the opposite); b) acceleration electric field (longitudinal) leaves the electron polarization unchanged; c) transverse magnetic field rotates the direction of the beam at the same rate as the electron spin, so that a magnetic field leaves the state of transverse polarization unchanged; d) longitudinal magnetic field does not change the direction and magnitude of the momentum but the electron spin precesses about the propagation axis.

The possibility to rotate by angle Ψ the electron spin by a magnetic field is described by the following equations [27], which correspond to c) and d) cases:

$$\Psi_{\parallel} = \frac{e}{E}\left(1 + \eta_g \frac{\chi}{1+\chi}\right)\left|\vec{\sigma} \times \vec{B}_{\parallel}\right| l \tag{4}$$

$$\Psi_{\perp} = \frac{e\eta_g}{mc^2}\left(1 + \frac{1}{\chi}\right)\left|\vec{\sigma} \times \vec{B}_{\perp}\right| l, \tag{5}$$

where $\vec{\sigma}$ is the unit vector of the spin, E is the energy, $\eta_g = (g-2)$ is the gyromagnetic factor of free electron, and χ denotes the electron charge-to-mass ratio. The components of the magnetic field are according to the particle beam path.

From the described influence of the slowly varying electric and magnetic field on the spin we come to the conclusion that the longitudinal polarization of the e^+ created in the bulk of the converter will be transformed to transversal polarization as the e_s^+ are extracted perpendicular to the γ-beam axis. The consequent focusing will not change the direction or the degree of the polarization. Due to the solenoidal magnetic field in the transport line the e^+ spins will rotate along the solenoid axis but the degree of the initial beam polarization will be preserved.

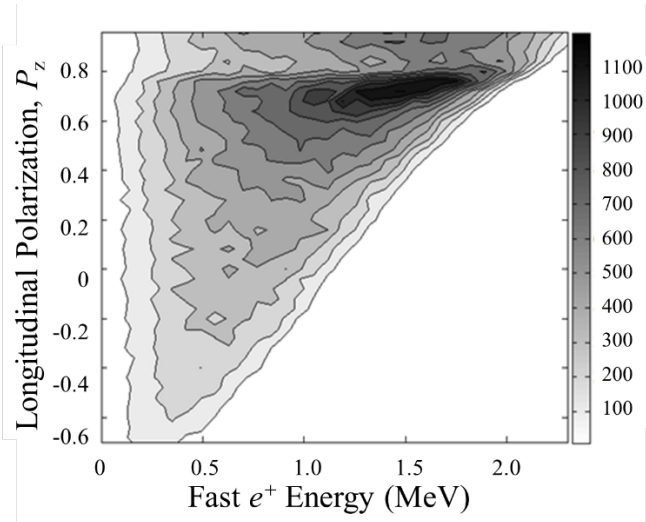

Fig. 24 – Longitudinal polarization as a function of the energy of the fast e^+ as created in the bulk.

To clarify how the circular polarization of the γ-beam is transferred to e_s^+ spin polarization we had performed Geant 4 simulations for the proposed target geometry (see Section 2.1.3) which is optimized for the best moderation efficiency. The analysis was separated into two parts: the polarization of the fast e^+ created in the bulk and the polarization of the e_s^+. The longitudinal polarization of fast e^+ created in the bulk of the converter as a function of the fast e^+ energy is plotted in Fig. 24. It can be seen that the fast e^+ with lower energy carry less helicity. The longitudinal polarization degree of the fast e^+ is 39%. The results in Table 2 show how the polarization degree is affected by selected energy cuts. Actually, the energy cut is the main method applied for the polarized e^+ production in Large Colliders projects proposals. The same method was used by House and Zitzewitz, by introducing an absorber between the e^+ source and the moderator [21].

Table 2

Degree of polarization at selected energy cuts of the fast e^+ calculated from the data shown in Fig. 24.

e^+ energy cut (keV)	0	350	700	1050	1400	1750
Degree of polarization (%)	46.7	49.0	56.4	65.7	74.9	82.8

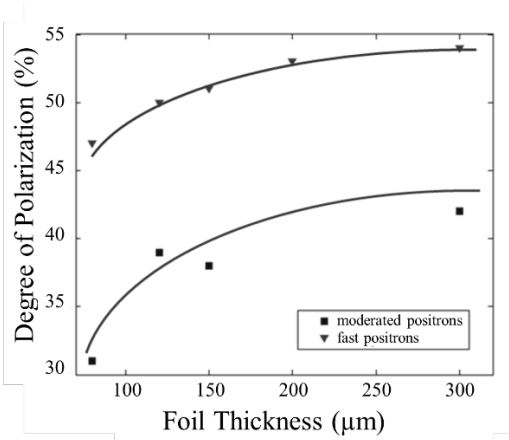

Fig. 25 – Degree of polarization of the fast e^+, which escape the converter, and of the e_s^+ as a function of the foil thickness, at fixed geometry parameters of the converter. The large data scattering for the e_s^+ is due to low statistics, as a result of the low moderation efficiency. The lines are guide for the eye.

Due to the fact that the low energy e^+ are moderated with higher efficiency compared to the high energy e^+ there is a difference between the degree of polarization of fast e^+ and e_s^+. The effect of the foil thickness is clearly seen in Fig. 25. The effect on the fast e^+, which escape from the converter, is due to the fact that by increasing the foil thickness, the absorbance of low energy γ-rays, which carry low polarization degree is increased, giving a better contribution of γ-rays of higher energy and thus of higher polarization degree.

The effect of the foil thickness on the degree of polarization of the e_s^+ is twofold. First, is the increased degree of polarization of the fast e^+, and second, a thicker foil absorbs better the low energy fast e^+, which carry low polarization, and they do not reach the near surface region to be emitted as e_s^+. However, this lowers the moderation efficiency, as can be seen in Fig. 26.

The demand for high intensity polarized e^+-beam was established long time ago [29]. Applications include studies of the moderation process, surface and bulk magnetism, and optically active molecules.

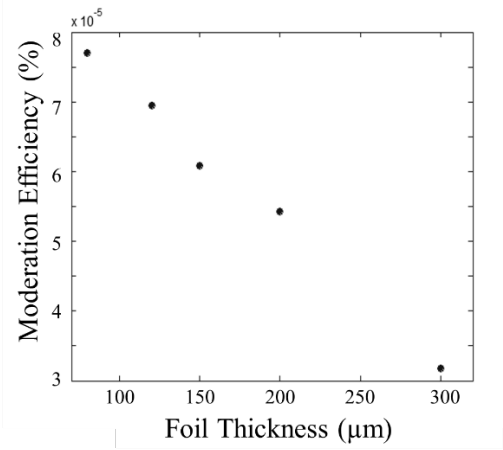

Fig. 26 – Moderation efficiency as a function of the foil thickness at fixed other geometry parameters of the converter.

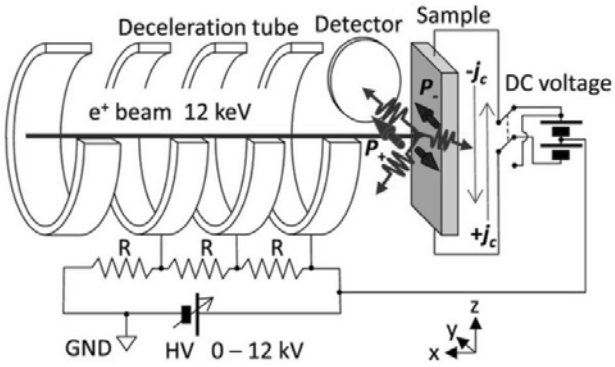

Fig. 27 – Transversely polarized e^+ are injected into the center of the sample under a direct current ($\pm j_c$). The beam energy of 12 keV is reduced to 50 eV by a deceleration tube. The γ ray detector is perpendicular to the beam axis. Reproduced with permission from [28].

Positrons with well-defined spin orientation will be of great help for investigations of magnetic materials and surface magnetism. For instance, Fig. 27 shows that, when interacting with a magnetic surface, a flux of very slow (50 eV) e^+ with transverse polarization, prior to their annihilation with the electrons belonging to the outermost layer, will eventually form short lived (125 ps) *p*-Ps, for which the electron and e^+ spins are antiparallel (↑↓), depending on the polarization state of the electrons. The lifetime of *o*-Ps, for which the electron and e^+ spins are parallel (↑↑), is by three orders of magnitude longer (142 ns). Therefore, PALS technique should

be able to derive separately these events. Controlling the DC current direction the spin orientation of the electrons from the outmost sample surface can be changed. It follows that a direct picture of the density of spin up and spin down electrons may be derived by such measurements. CDBS technique is also sensitive to para- and *o*-Ps because *p*-Ps self-annihilation contributes with low momentum to the e^--e^+ momentum distribution.

2.4 COINCIDENCE DOPPLER BROADENING SPECTROSCOPY

Due to the fact that prior the annihilation the e^+ is thermalized, the electron high momentum part determines the e^-- e^+ annihilation momentum and it can be used to identify the chemical surrounding of the annihilation site [30,31,32]. This is based on the fact that tightly bound core electrons, preserve their element-specific properties even in a solid. For the Doppler Broadening Spectroscopy (DBS) the longitudinal Doppler shift is registered by a single HPGe detector. The frequency of the Doppler shifted γ-quanta is given by the following equation:

$$\nu_{\text{blue, red}} = \nu_0 \sqrt{\left(1 \pm \frac{V_l}{c}\right) / \left(1 \mp \frac{V_l}{c}\right)} \approx \nu_0 \left(1 \pm \frac{V_l}{c}\right), \tag{6}$$

where $\nu_0 = m_0 c^2/(2h)$ and V_l is the longitudinal projection of the electron velocity. Since V_l is only a projection and the electrons are not mono-energetic we observe Doppler broadening. The broadness is hence a value for the velocity distribution of the electrons at the annihilation sites.

The technique of Coincidence Doppler Broadening Spectroscopy is based on the coincident detection of both 511-keV annihilation γ-quanta from a single annihilation event. This suppresses significantly the background, alloying observation of the electron high-momentum distribution.

Applying the standard coincidence technique with one high-purity Ge detector (HPGe) in coincidence with another γ-sensitive detector (such as a NaI scintillator) improves the peak to background ratio from about 10^2 up to 10^4 compared with a measurement using a single HPGe [30,33]. However, a superior technical realization of a coincidence experiment is the use of two HPGe detectors (Fig. 28) registering the energy of both annihilation quanta [32]. This results in a peak-to-background ratio of about 10^6 and an improvement of the energy resolution by a factor of $\sqrt{2}$.

Especially the high momentum wings of the 511 keV annihilation line depends on the chemical vicinity. In particular the core electrons maintain their atomic characteristic also in a solid making it possible to use the signal from the e^+ annihilation on core e^- for chemically selecting the atoms. Due to the much lower background of the CDBS the differences at the high momentum wings can be resolved and therefore, it is possible to identify not only the type of open volume defect, but also the atoms that surround the e^+ trap. The e^+ annihilation with core e^- has been studied both experimentally and theoretically [34] and the references

therein. The chemical selectivity of the e^+ probe is well demonstrated. The most common way to enhance the differences due to the chemical surrounding of the e^+ trap is to represent the momentum distribution as a ratio to a reference element.

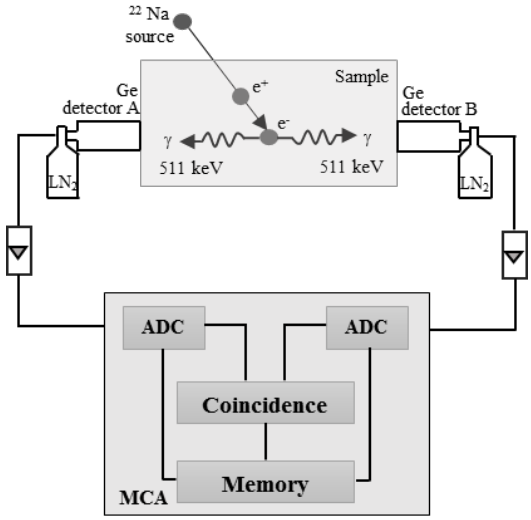

Fig. 28 – Scheme of the Doppler-broadening coincidence spectroscopy. Both collinear γ-quanta are detected by two HPGe detectors. A coincidence unit ensures that only those events are stored in the memory that are caused by the same annihilation event.

The combination of chemical sensitivity of CDBS and depth profiling with monoenergetic e_s^+ opens large area of opportunities in material science to study defects.

2.5 GAMMA-INDUCED POSITRON ANNIHILATION LIFETIME SPECTROSCOPY

Accelerated e_s^+ up to 40 keV or those generated by isotopes undergoing β^+ decay (like the common used ^{22}Na) can probe a sample depth of only few µm to few mm. However, in many cases, determination of concentration and types of defects for the entire volume of bulky samples is of interest. The method of γ-induced Positron Spectroscopy (GiPS) has been demonstrated at a normal-conducting 200 Hz linear accelerator [35] and UVSOR-II electron storage ring [36]. Unique setup for e^+ annihilation spectroscopy has been established and optimized at the superconducting linear electron accelerator ELBE at Helmholtz-Zentrum Dresden-Rossendorf (Germany). The intense, pulsed (up to 26 MHz) photon source (bremsstrahlung with energies up to 16 MeV) is used to generate e^+ by means of pair production throughout the entire sample volume. Due to the very short γ-ray bunches (shorter

than 5 ps temporal length) and controllable repetition frequency, the facility provides excellent conditions for GiPS, where both Aged Momentum Correlation and Coincidence Doppler Broadening Spectroscopies are realized [37]. The γ-beam time structure (see Section 2.1.1) at ELI-NP is fixed and provides much less time averaged number of micro bunches (3.2 kHz). Unfortunately, the gaps of 16 ns between the micro bunches are too short for a HPGe detector to be able to segregate signals arising from annihilations of different micro bunches. Therefore, only fast detectors can be used.

Due to the fact that the optimized γ-to-e_s^+ converter will stop less than 50-70% of the γ-rays we propose to build simple and cost effective separate Gammas induced PALS (GiPALS) which will use the passed through the converter γ-rays and will work simultaneously with the slow positron beam system. The temporal beam structure is maintained during the process of Compton scattering resulting in a photon beam consisting of pulses with less than 1 ps duration. Positron generation inside the sample takes place immediately within this short time, so the accelerator signal for electron bunch generation can be used as start signal for e^+ lifetime measurements. Positron lifetime spectroscopy is realized by measuring the time difference between the accelerator bunch pulse and the annihilation γ-rays detected by a fast detector. The fixed gap of 16 ns between bunches determines the spectrometer time range, thus limiting the lifetimes which will be possible to be measured to approximately 5 ns.

2.6 POSITRON ANNIHILATION LIFETIME SPECTROSCOPY

The lifetime of a thermalized e^+ depends on the electron density in its vicinity. The cross-section σ for the annihilation is given by [38]:

$$\sigma = \pi r_0^2 \, c/v_{e^+}, \tag{7}$$

where $r_0 = e^2/(m_0 c^2)$ is the classical electron radius and v_{e^+} is the e^+ velocity. The lifetime of the positron τ_{e^+} is calculated from the cross-section as

$$\tau_{e^+} = \lambda_{e^+}^{-1} = (\sigma v_{e^+} n_{e^-})^{-1}. \tag{8}$$

The e^+ annihilation rate λ_{e^+}, which is the inverse of the lifetime, is proportional to the electron density n_{e^-}. Thus, at places with lower electron density (like open volume defects) compared to that of a perfect lattice the e^+ is trapped and lives longer. In general, the larger the open volume defect, the lower the electron density and hence the longer the e^+ lifetime. For an exact calculation of the e^+ lifetimes the two-component density-functional theory, together with the local density approximation can be used [39].

In materials with low electron density a e^+ may form Positronium (Ps) with an electron prior to the annihilation. Ps is a bound state of a e^+ and an e^-. Corresponding

to the mutual spin orientations (anti-parallel and parallel) of the consisting particles, Ps exists in two states, called *para*-Ps (*p*-Ps) and *ortho*-Ps (*o*-Ps). The intrinsic lifetimes of *p*-Ps and *o*-Ps in vacuum are 0.125 and 142 ns, respectively. In molecular materials, such as polymers, the Ps is localized in free-volume holes, or cavities. The pick-off annihilation process shortens the *o*-Ps lifetime to some ns. The pick-off annihilation lifetime of the *o*-Ps is directly correlated to the size of the free-volume holes by a semi-empirical equation proposed by Nakanishi and Jean [40] according to the quantum-mechanical model of Tao [41], later developed by Eldrup *et al.* [42]. The equation correlates the radius, *R*, of the spherical free-volume hole where Ps is confined, to the *o*-Ps pick-off annihilation lifetime. Goworek *et al.* [43] extended the Tao-Eldrup model by accounting for the possibility of Ps to annihilate from exited states not only from its ground state. However, the calculations include Bessel's functions, and due to their complexity this model is not in common use. Based on the same idea Gidley *et al.* [44] have proposed a simple formula to calculate the *o*-Ps lifetime in a rectangular pore. For large pores, Ps behaves like a classical particle and the *o*-Ps lifetime is directly correlated to the classical mean free-path of a particle. The sizes of pores with different shapes (cylindrical, spherical) can be determined from the mean free-path. This model is known as Extended Tao-Eldrup model (ETE) and is used in e^+ spectroscopy porosimetry. The applicability of PALS to study a variety of materials and the typical observed lifetimes is schematically presented in Fig. 29.

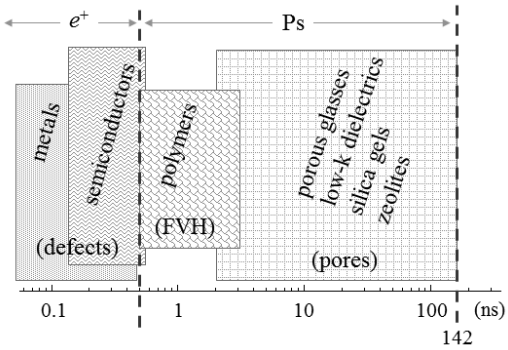

Fig. 29 – Range of materials for which PALS is applicable and the typical observed lifetimes.

For PALS a start and a stop signal is needed to register the birth and death of a e^+. In the conventional PALS a e^+ source, attached in sandwich geometry to the specimen, is used. In the case of ^{22}Na e^+ source, the prompt nuclear γ-quanta of 1275 keV detection starts and one of the annihilation quanta of 511 keV stops the clock. The disadvantage of the conventional PALS is the relatively deep and uncontrollable mean penetration depth of e^+ (few hundreds of μm up few mm).

Using a e^+-beam the incident energy can be controlled and hence depth dependent measurements can be performed. However, another way to start the clock for PALS is necessary. One possibility is to use a pulsed beam and to derive the signal from the master clock of the pulsing system. The generated e^+-beam via pair production have the same pulse structure of the incident γ-beam with a pulse width in the picosecond range. The first question to be answered is if this time structure can be directly used for e^+ lifetime experiments situated in the positron laboratory hall, or in other words, if the time structure can be preserved after transportation of more than 10 meters away from the high radiation field in the environment of the converter. The e_s^+ are produced by the moderation and they are emitted from the moderator with an average energy of about $\varepsilon_+ = 3$ eV (W – moderator). But, even from a well annealed moderator foil an energy uncertainty $\Delta\varepsilon_+$ of about ± 0.2 eV and a low energy tail is observed [45]. In order to obtain as much e^+ as possible a stack of first moderator foils (converter) has to be used. The point of creation is totally smeared out and will be 30 cm long. Also the primary e_s^+-beam, after focusing from the converter, is expected to have a diameter in the order of centimetres. The time spread Δt (FWHM) (of the initial pulse of positrons of few ps after a flight path of 10 m) is dependent on the extraction energy and easily reaches values greater than 1 ns, which is already too long to be used for timing. The large length of the converter and the necessity to focus a large diameter beam to a small spot on the target will cause additional time spreads. The most important factor is that segmentation of the converter, which is proposed for the efficient extraction of the e_s^+ (see Section 2.1.3), will totally distort the initial time structure due to the fact that the applied electric field will introduce additional energy spread of few tens of eV. The conclusion is that the pulsing time structure will be lost and the primary beam transported in the laboratory hall will be quasi continuous. Consequently, to achieve a pulsing beam the chopping and bunching technique has to be applied.

Another possibility for start signal is to detect the secondary electrons which are kicked out from the sample by the incident e^+. The advantage of the pulsing system is that the count rate is sample independent and the timing resolution that can be achieved is better compared to the conventional systems. Disadvantage is the complicated design for beam bunching and loss of beam intensity. The tagging by secondary electrons works with continuous beam and provides excellent 10^6 peak to background ratio which gives the possibility to be measured very long lifetimes (of the order of 100 ns) with low relative contribution (less than 1%).

2.7 AGED MOMENTUM CORRELATION SPECTROSCOPY

The age-momentum correlation studies are based on simultaneous detection of the two quantities which can be observed by annihilation of an individual positron in matter the positron age τ (measured by PALS) and the momentum p of the annihilating positron-electron pair (measured by DBS). The correlations between τ

and p allows us to follow directly transitions between different positron states like trapping of positrons, chemical reactions of positrons and positronium. The advantage of implementation of AMOC technique at pulsed slow positron beam is not only the selective depth of keV positrons but also the count rate improvement due to avoiding the triple coincidence needed for isotope based AMOC. An example of AMOC spectrum is shown in Fig. 30. Sections of constant positron age represent energy spectra at different positron ages. Summation over all channels with constant energy or constant positron age results in positron lifetime spectrum or the Doppler broadening spectrum, respectively.

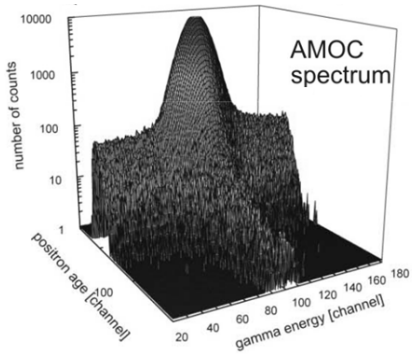

Fig. 30 – Example of AMOC spectrum.

For better visualization of the AMOC data a time dependent S-parameter, the so-called lineshape function $S^t(t)$ is often used to demonstrate changes in the population of different positron states as a function of positron age. A plot of the mean positron lifetime τ as a function of the photon energy (known as "Tsukuba plot") is another simple visualization possibility [46].

The AMOC data (two-dimensional) can be fit directly by a model. The models for the processes under investigation are described by appropriate system of rate equations with suitable initial conditions, and convoluting it with the time and energy resolution function of the set-up. Parameters derivable from such two-dimensional data analysis are: (i) the annihilation rates and the Doppler broadening linewidths of all positron states involved, (ii) the transition rates between distinct positron states, and (iii) the fraction of positrons forming positronium.

2.8 POSITRON ANNIHILATION INITIATED AUGER ELECTRON SPECTROSCOPY

Positron induced Auger Electron Spectroscopy (PAES) has a higher surface sensitivity (most of the implanted e_s^+ are trapped at the surface bound states and annihilate with electrons in the topmost atomic layer) and a higher signal to noise

ratio at the Auger-transition energy (there is no collision-induced secondary electron background produced in the higher energy range of released Auger-electrons) than Auger electron spectroscopy (AES), being one of the most powerful technique used for studies on the elemental composition of the topmost atomic layer of a surface [47, 48, 49]. In PAES, some of the e^+ from a low-energy (few tens eV) and high intensity e^+-beam implanted into a solid are trapped in a potential well at the surface and annihilate the inner atomic shell electrons, creating core excitations, resulting in emission of Auger electrons [47], which are detected by an electron energy analyzer, preferably with high energy resolution. PAES is considered a non-destructive analysis method and is the only method to detect open volume defects [50].

The time-of-flight spectrometer is designed so that it should allow short measurements time for the PAES spectra, by collecting the Auger electrons emitted in a solid angle of 2π around the sample (compared with a solid angle of about 0.1% for classical hemispherical energy analyzers) [48, 49]. The electron time-of-flight is considered the time between the annihilation radiation at the sample and when the electron hits the detector [49]. According to Hugenschmidt *et al.* a time of flight (TOF)-PAES spectrometer consists of a trochoidal filter and a flight tube in a Faraday cage, designed so that it can achieve an improved energy resolution of approximately 1 eV at high electron energies up to about 1000 eV [49]. While the main drawback of PAES is the low intensity of the e_s^+, with the e_s^+ flux being five to eight orders of magnitude lower than the electron current of an electron gun [49], in case of TOF-PAES the main drawback is the low energy resolution (*e.g.*, 2 eV at $E_+ = 60$ eV).

The use of beams of polarized positrons enables a new spectroscopy method for investigations of magnetic surfaces: polarized positron annihilation initiated Auger electron spectroscopy (P-PAES) [51, 52]. The ability of positrons to create polarized core holes stems from the fact that the annihilation rate for spin singlet collisions with core electrons is many times faster than for spin triplet collisions in the energy ranges involved in PAES (Fig. 31). Indeed, in vacuum the *o*-Ps (↑↑) has a lifetime of about 142 ns, to be compared with the lifetime of *p*-Ps (↑↓), 125 ps. As a consequence, the annihilation occurs three orders of magnitude faster with electrons of opposite spin than with electrons whose spin is parallel to the positron spin. In the following, we shall extrapolate this result from vacuum towards annihilation with core electrons, but note also that the detailed study of the branching ratios between annihilation channels starting from singlet and triplet state would be a quite interesting study in itself (*e.g.*, as function on the binding energy of the core electrons, hence on the relative velocity of the electron and the positron). Moreover, in the case of solids the number of gammas emitted from the *o*-Ps annihilation (usually three, from charge conjugation considerations) might vary, since the solid could take over some recoil momentum in the form of phonons, polarons, *etc*.

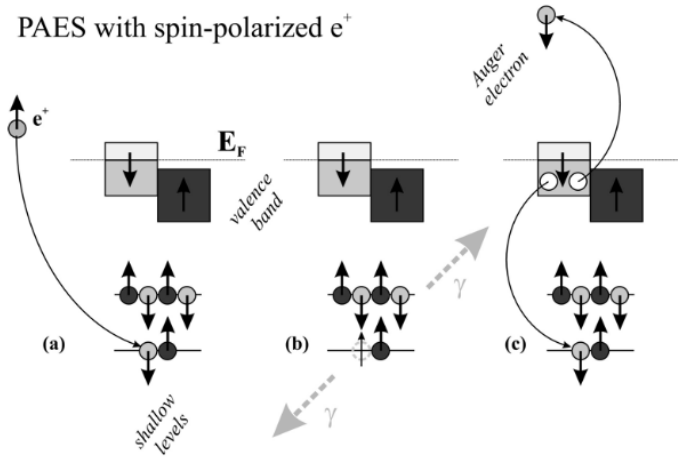

Fig. 31 – Principle of positron annihilation induced Auger electron spectroscopy (PAES), starting with spin-polarized positrons.

As a consequence of the simplified assumptions from above, the probability for a positron to annihilate with an electron with opposite spin is about three orders of magnitude larger than the probability to have this process occurring from a triplet electron-positron state. Thus, it is expected that a beam of polarized electrons creates a population of polarized core holes with a polarization oriented in the same direction as that of the positrons.

This population of polarized core holes serves as starting point for the Auger process. Shallow core holes will mainly be filled by valence electrons and, in absence of spin flip processes, the electron filling the core hole will have opposite spin to that of the core hole (Fig. 31), *i.e.*, opposite spin to that of the positron, no matter which is the spin orientation of the ejected Auger electron. Thus, studying the yield of Auger electrons one will directly investigate the valence band density of electrons with spins opposed to the spin of the positron. Indeed, spin-polarized Auger electron spectroscopy was proposed to yield such information [53], but in this case one needs a further discrimination of the spin of the emitted Auger electron via a Mott detector (whose efficiency ranges between 10^{-3} and 10^{-4}), whereas in the actual case, if one uses beams of polarized positrons, practically the whole yield of Auger electrons originates from spin-resolved processes. Also, the complete interpretation of spin resolved Auger electron spectroscopy is hampered by screening and electron correlation effects.

In fact, the spin dependence of correlation effects have to be considered also in this case [39], though via a simpler formalism; eventually, these effects can be

expected to provide additional information about magnetic surface systems and the Auger process [51].

A variety of science cases are interesting to be studied by means of PAES:

A. Conventional PAES

A.1. Buried Ni islands under the Cu (001) surface in the sub-monolayer regime. This process was investigated so far by medium energy ion scattering [54], which is a method where the surface is interacting with the ion beam used for investigation. Thermo-magnetic measurements revealed that the magnetic (Ni) islands have a two dimensional character [55]. PAES may be used to mitigate on the real position of Ni atoms in real time (*i.e.*, during Ni deposition at various temperatures) and also on the 2D character of these islands. Such experiments might also be coupled with spin-resolved techniques.

A.2. Studies of atomically clean, free ferroelectric surfaces. Recently, the synthesis of well-ordered ferroelectric surfaces was successful with no C contamination and visible LEED patterns [56, 57]. States with different out-of-plane polarizations will repel differently incoming positrons, therefore PAES could be a valid method to derive the surface termination (and composition) with sensitivity to its polarization state. Up to now, such experiments were performed by using photoelectron spectro-microscopy, with the limitation that not all core levels were available, thus no complete picture of the surface composition could emerge [56].

A.3. PAES diffraction used to study surface relaxation and rumplings in ferroelectrics. For instance, standard photoelectron diffraction of such surfaces exhibited diffraction patterns, but whose interpretation was difficult, owing to the need to take into account multiple scattering events, with photoelectrons originating from several layers from the surface [58]. By using PAES electrons whose origin is clearly from the outermost layers, the simulation of diffraction patterns will be considerably simplified. For these experiments, collection of PAES electrons with an angular resolved scheme is necessary. This can be achieved, *e.g.*, by using a fragmented detector on the rear part of the microchannel plate assembly.

A.4. Selective adsorption of polar molecules on ferroelectric surfaces. Recently, from X-ray photoelectron spectroscopy it was inferred that contaminants (fatty acids) adsorbs mostly on ferroelectric areas exhibiting outwards ($P^{(+)}$) polarization [59]. However, the method used was just conventional photoelectron spectroscopy; it is highly desirable to use for such investigations a method allowing one to investigate the outermost layer deposited on the surface. Additionally, this study may be supplemented with experiments of *in situ* poling of the ferroelectric surface, such as to quantify exactly the area covered by adsorbates. This study could have a considerable impact in the area of tunable catalysis [60].

A.5. Interface properties of oxide hetero-structures. The origin of 2D superconductivity in the electron gas confined to a thin sheet at the interface between two insulating dielectric oxides, *e.g.*, $LaAlO_3$ and $SrTiO_3$, [61] is still not well understood, the experimental data suggesting a clear implication of the structural

defects present at the interface or within the component layers. Positrons being sensitive to defects and composition of interface regions in polar hetero-structures [62,63], the correlation between the electronic properties and interface characteristics of the $LaAlO_3/SrTiO_3$ hetero-structure(s) can be studied by means of PAES. The surface stoichiometry of the deposition front can be studied without compositional chances induced by the interaction of the e_s^+-beam with the analyzed surface, the evolution of the stoichiometry at the growth front can then be correlated with the final electrical transport properties of the hetero-structure.

A.6. Graphene and graphene-like single atomic layers. The complete coverage of a surface with graphene or with graphene-like layers is still a matter of debates today, but one assists also to a wide diversification of the monolayer materials whose synthesis was successful. For instance, recently other materials (*e.g.*, BN) were grown by our groups in graphene-like structures [64]). PAES could bring significant insight on the continuity of these graphene-like layers, as combined with scanning tunneling microscopy (STM). Note that the NIMP and Elettra teams are on the way to be admitted in the Graphene Flagship project.

B. Using spin-resolved positrons

B.1. Orientation of surface magnetic moments. Even for ferromagnetic Fe(001) or Ni(001) single crystals, it may happen that the outermost layer has a different orientation of magnetic moments with respect to the bulk [65]. One speaks about ferromagnetic or antiferromagnetic coupling of the surface layer to the inner (bulk like) layers [66] or, in some cases, about the formation of a magnetic ‘dead layer’ at the surface. For rare earths, the situation is even more complicated and detailed explanation of the surface magnetism of these materials is hindered by the ability to investigate their ‘real’ surface magnetism [67].

B.2. Indirect exchange interaction at surfaces. The indirect exchange intermediates the magnetic coupling between spins via charge carriers from localized or delocalized orbitals [68]. In solid metals, this interaction is usually denoted by RKKY (Ruderman-Kittel-Kasuya-Yosida). This interaction is dependent on the dimensionality of the system and indeed it was shown that in the case of 2D surfaces and relatively low electron densities a much stronger ferromagnetic coupling occurs as compared with the 3D case [69]. Such purely 2D investigations may be undertaken by using PAES with spin resolved positrons. Layers formed by 2D RKKY systems could be a valid alternative to high magnetic energy density materials.

B.3. Current induced spin polarization. Recently, it was demonstrated the ability of spin polarized positrons to probe surface spin polarization in non-magnetic metals, where this effect was mainly explained via a spin-orbit coupling mechanism [28]. To date, no such experiment was reported by using ferromagnetic materials or ferromagnetic layers, despite the expected stronger exchange or Hubbard interaction, when compared to the spin-orbit interaction.

B.4. Multiferroicity is the coupling between ferroelectricity and ferromagnetism, most usually through lattice strains or more subtle electronic mechanisms [70]. On the other hand, ferroelectric thin layers exhibiting out-of-plane polarization feature also an accumulation of mobile charges near surface, in order to compensate the depolarization field [71]. It might be expected that this almost 2D carrier gas could be used to intermediate exchange between surface magnetic moments, yielding RKKY (or Zener) mediated multiferroicity (see Topic B.2 above). Spin-resolved magnetic densities of carriers could be measured as a function of the ferroelectric polarization state (see Topic A.2 above).

3. TECHNICAL PROPOSAL

3.1 LOCATION OF THE EXPERIMENTAL SETUP

All elements of the Positron Spectroscopy laboratory will be situated in the AE1 and E3 halls of the ELI-NP building (see Fig. 32). In the AE1 area the converter interaction chamber with the focusing system for the primary slow positron beam will be installed at approximately 4 m after the interaction point of creation of the low energy γ-beam.

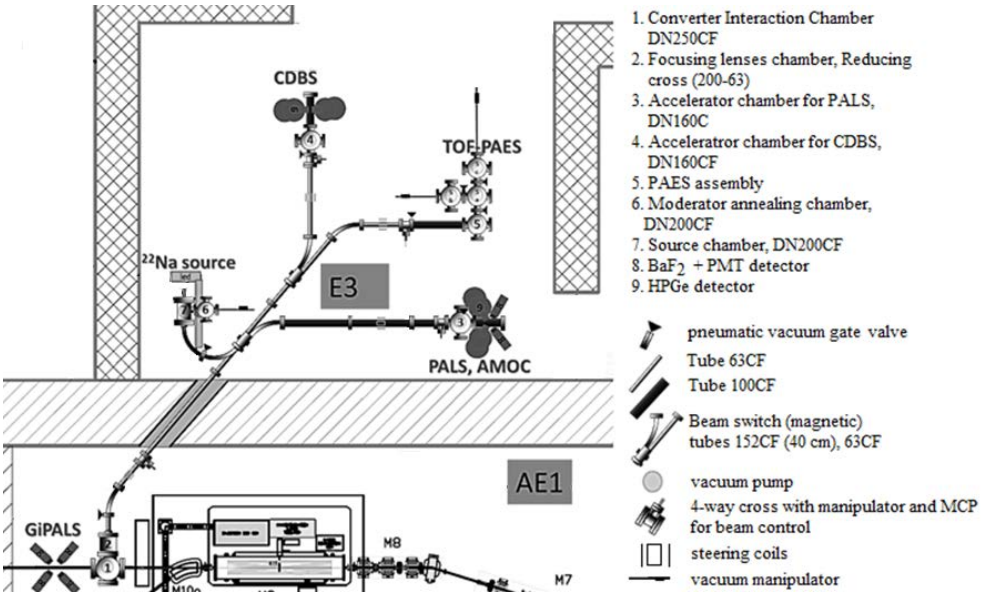

Fig. 32 – Scheme of Positron Spectroscopy Laboratory elements situated in halls AE1 and E3 of the ELI-NP building.

The detector assembly for the GiPALS will be placed in air, after the converter interaction chamber. The primary beam will be guided through a hole in the wall between the AE1 and E3 halls. The radioactive source chamber and the CDBS, PALS and PAES spectrometers will be built in the E3 hall.

3.2 CONVERTER TEMPERATURE, MACHINING AND ANNEALING

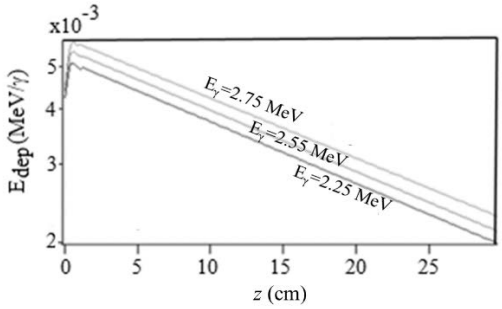

Fig. 33 – MCNPX calculation of the energy deposited per γ-ray $E^{\gamma}_{\mathrm{dep}}$ in each of the 144 tungsten foils, for 2.25 MeV, 2.5 MeV and 2.75 MeV γ-rays incident on the converter as function of their position Z along the converter length.

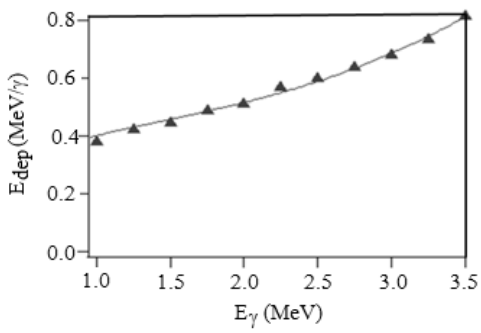

Fig. 34 – MCNPX calculation of the energy deposited per γ-ray $E^{\gamma}_{\mathrm{dep}}$ in the converter assembly as function of the γ-ray energy.

For a precise choice of how the converter should be machined and for a design of the converter segmentation it is necessary to estimate the temperature of the converter during operation. The most important is to find an answer to the question if the converter needs active cooling. The estimate of the converter temperature was done in two steps. First, MCNPX software [72] was used to find the energy deposited

in the converter by the incident γ-rays. The geometry sizes of the converter were taken as they were found after the optimization for best conversion efficiency (H = 6 mm, W = 16 mm, d = 0.08 mm, G = 2 mm, N = 144, L =30 cm, see Section 2.1.3). Due to the fact that γ-rays with $E_\gamma < 1.022$ MeV will be eliminated by collimation they will not be taken into account. In Fig. 33 we can see the effect of γ-ray attenuation on the energy deposited by γ-rays in the foils of the converter according to its position Z along the converter length. The energy deposited in the entire converter assembly per γ-ray $E^{\gamma}_{\mathrm{dep}}$ as a function of the γ-ray energy is plotted in Fig. 34. Using the data of the γ-beam energy spectra presented in Fig. 3 we calculated the relative number of γ-rays per bunch $\Delta n_{\mathrm{k}}/n_0$ for $1.0 < E_\gamma < 3.5$ MeV divided into 10 intervals. The data is summarized in Table 3. The energy deposited in the entire converter assembly per bunch is calculated by $E^{\mathrm{bunch}}_{\mathrm{dep}} = n^{\mathrm{bunch}}_{\gamma} \sum_{\mathrm{k}} E^{\gamma_{\mathrm{k}}}_{\mathrm{dep}} \Delta n_{\mathrm{k}}/n_0 = 7.45 \times 10^6 \times 0.396$ MeV or $E^{\mathrm{bunch}}_{\mathrm{dep}} = 0.472 \times 10^{-6}$ J. Consequently the deposited power will be $P_{\mathrm{dep}} = 3200 \times 0.472 \times 10^{-6} = 1.5 \times 10^{-3}$ J s^{-1}.

Table 3

Relative number $\Delta n_{\mathrm{k}}/n_0$ of γ-rays and the energy deposited in the converter assembly for 10 intervals of γ-ray energy.

k	$E_{\mathrm{k-1}}$ (keV)	E_{k} (keV)	$E^{\gamma_{\mathrm{k}}}_{\mathrm{dep}}$ (MeV)	$\Delta n_{\mathrm{k}}/n_0$
1	1000	1250	0.424	0.02192
2	1250	1500	0.4474	0.0571
3	1500	1750	0.4879	0.05522
4	1750	2000	0.5119	0.05535
5	2000	2250	0.5697	0.05751
6	2250	2500	0.599	0.06168
7	2500	2750	0.6376	0.06787
8	2750	3000	0.6809	0.07608
9	3000	3250	0.7341	0.08631
10	3250	3500	0.7854	0.09855

The calculation of the temperature in the tungsten converter was done in COMSOL, using the power lost by γ-rays inside each tungsten foil. The energy is not distributed uniformly in the volume of the W foil because the γ-beam has a Gaussian profile with a cylindrical cross-section. For this reason, it is necessary to study the change in the equilibrium temperature with the transversal area of the γ-beam, measured on the surface of the foils. For simplicity, we consider that the beam hits a central rectangular area (height h_{c}= 5 mm and width w_{c}= 5 mm) in the middle of the transversal foils (see Fig. 35). The deposited power per foil is

$P_{\mathrm{dep}}^{\mathrm{foil}} = 0.104\times10^{-4}$ W which gives the power density in the central rectangular part of 5.2×10^{-6} W m^{-3}. The deposited power per unit volume in MCNPX was the input value for temperature calculation using "Heat Transfer in Thin Shells" (COMSOL). The initial temperature of the converter was set to 293 K. The radiative loss of heat was taken in account with the "Surface to ambient radiation" node in the "Heat Transfer in Thin Shells". The surface temperature at equilibrium is given in Fig. 35 and we can conclude that no active cooling is necessary for the converter assembly as the maximum temperature excesses the ambient one only by 2 K. Even if we consider that foils situated close (small z) to the γ-beam entrance will be subjected to approximately 2 times higher deposited energy as compared to the averaged one (see Fig. 33) the conclusion remains valid.

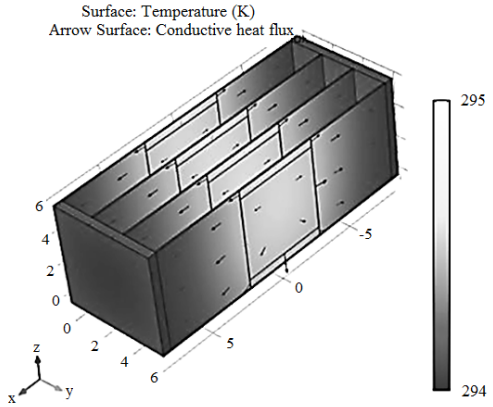

Fig. 35 – Surface temperature of a model of the tungsten converter as simulated by COMSOL.

However, due to the necessity to use the insulating sheets, *in situ* high temperature treatment of the converter assembly will not be possible. Therefore we have to apply the well-known method to anneal *ex-situ* the tungsten sheets at approximately 2000 °C in good vacuum and partial oxygen atmosphere and afterwards to assemble the CMA.

3.3 ISOTOPE SOURCE

We propose to use a commercial e^+ source ^{22}Na of 1.85 GBq activity. The radioactive material is in a special titanium capsule for UHV (see Fig. 36). This capsule will be mounted on short linear manipulator and its working position will be in a central hole of a solid thick cylinder of Fe-Cu alloy (for γ-ray shielding) placed in the vacuum chamber (5-way cross DN200CF, see Fig. 37). The moderator will be a set of 10-20 tungsten meshes on a holder mounted on a long linear and rotatable

transfer manipulator. In a second chamber (5-way cross DN 200 CF) we will build an electron gun system for *in situ* contactless annealing of the moderator.

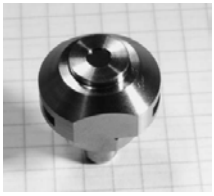

Fig. 36 – ^{22}Na capsule (iThemba) to be used as e^+ source.

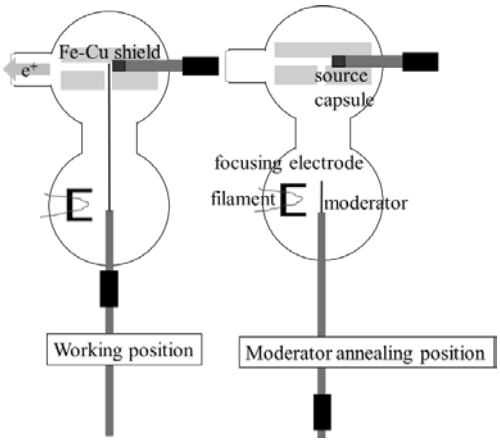

Fig. 37 – Sketch of the proposed source chamber. On the left the moderator is at working position in front of the source capsule, while on the right the moderator is at position for annealing.

3.4 CONVERTER CHAMBER AND BEAM FORMATION

The converter chamber drawings are represented in Fig. 38. It based on 6-way cross DN250CF. The γ-beam will enter from air to the vacuum through a thin window, part of the γ-rays will then interact with converter mounted on a manipulator (for alignments purposes) and the rest will exit the vacuum chamber through another thin window. The e_s^+ extracted from the converter will be focused by a system of electrostatic lenses.

The beam formation focusing system is copied from PULSTAR e^+ source [76] (see the geometry and field maps in Fig. 39). The lenses system has been designed for focusing of e_s^+ with longitudinal energy of up to 60 eV. The internal diameters of the lenses are 24.4, 20, 15.6, 11.2, 10, and 7.5 cm. The inner surface of lenses 2, 3 and 4 are tapered to improve focusing. The voltages applied to the lenses, empirically

found for best focusing, are reported as 800, 735, 50, −3100, 640 and 0 V. The exit grid of the moderator was at 910 V. Thus the e_S^+ are extracted with an energy of 1 keV. This design has been tested with electron guns out of the nuclear reactor core and good focusing of the e^+ emitted from a converter with diameter of 24 cm into a beam with diameter of 3.75 cm (FWHM = 2 cm) has been demonstrated [77].

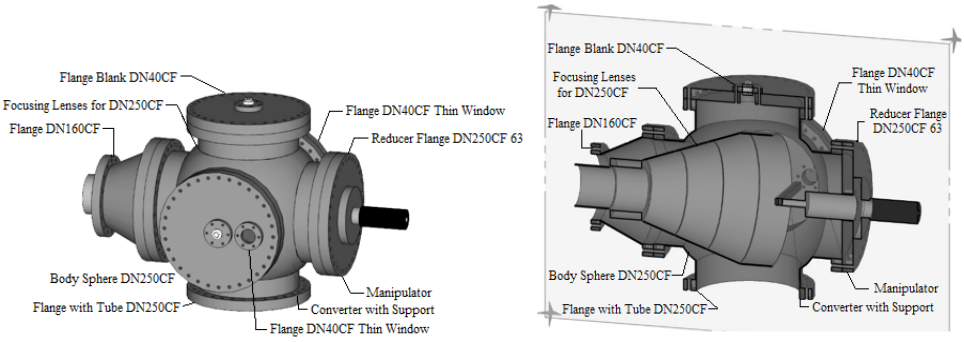

Fig. 38 – 3D sketch representation of the converter interaction chamber based on 6-way cross DN 250 CF. The right image gives a cross-section of the chamber with the plane normal to the incident γ-beam propagation direction.

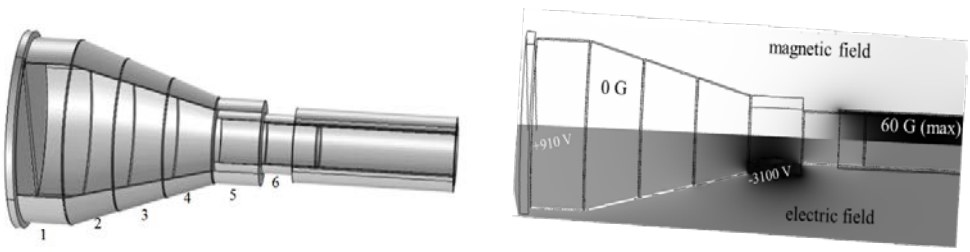

Fig. 39 – Geometry (left) and electromagnetic field potentials (right) of a system for beam focusing. Consists of six electrostatic lenses and the beginning of the solenoid for beam transport at magnetic field of 60 G.

The performance of the lenses system was simulated with COMSOL and the published results were confirmed (see Fig. 40). For a converter of 30 cm in length (or other) this system of lenses will be scaled (geometry sizes and potentials) to accept 30 cm in length source of e_S^+ and the beam size is expected to have a diameter of 4.7 cm (FWHM = 2.5 cm) as shown in Fig. 41.

We have to mention that we have simulated the focusing of the proposed system of electrical lenses in case the converter is in magnetic field, as it was described at the end of Section 2.1.4. The COMSOL simulations showed that magnetic field strength of 30-60 G deteriorate significantly the focusing capability

of the proposed system of electrical lenses. The conclusion is that extraction of e_s^+ in magnetic field is not compatible with the proposed focusing system for beam formation.

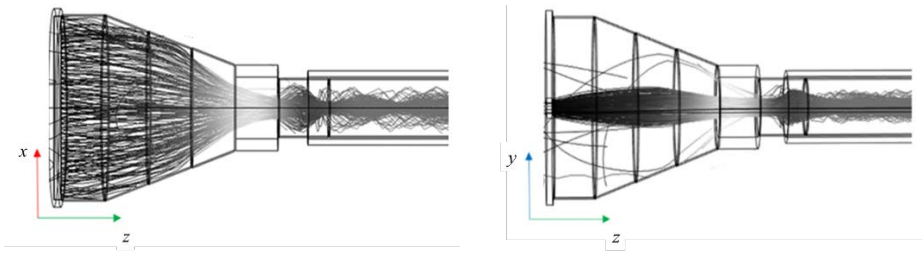

Fig. 40 – Projections in *x*-*z* plane (left) and *y*-*z* plane (right) of the e_s^+ trajectories in the system of lenses with the transport solenoid as simulated by COMSOL. The γ-beam propagates along the *x*-axis.

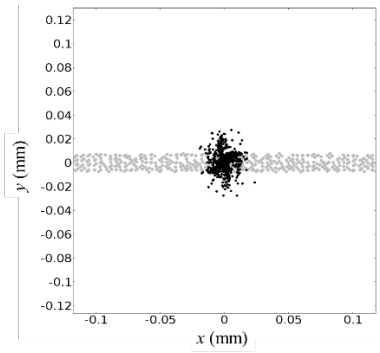

Fig. 41 – *x*-*y* position of e_s^+ at the initial inlet in grey and in the transport solenoid, after focusing, in black.

Further decrease of the beam spot size without losing from the e_s^+ intensity can be done by focusing with a non-uniform magnetic field, stronger at the sample position [78,79]. The principle of this kind of focusing is that a part of the longitudinal momentum is converted into transversal momentum and the problems which appear due to the fact that e^+ do not enter the sample in direction close to the normal are well-explained in [78]. The problems are increased fraction of backscattered e^+ and change in the implantation profile and these effects has to be carefully studied by simulations and taken into account in the analysis of the resulted spectra. The factor of beam spot reduction achieved by Falub *et al.* [78] is 5 times by using a strong NdFeB permanent magnet of 1.37 T behind the sample.

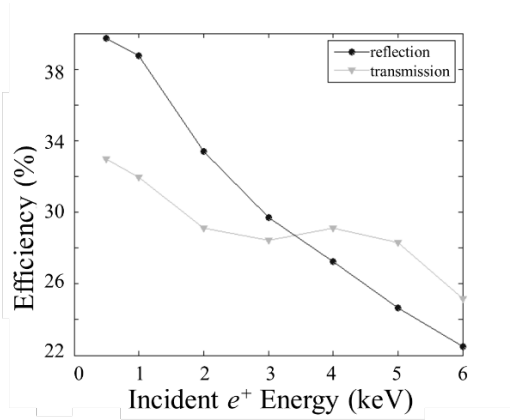

Fig. 42 – Maintaining positron intensity efficiency of re-moderation process. GEANT4 simulation results. For the reflection mode 2 μm-thick W is used. For the transmission mode 100 nm-thick W is used. In both cases the positron diffusion length was set to L_+=135 nm, which corresponds to W(100) single crystal.

The described beam formation results in a primary slow positron beam with rather wide spot. Without further beam size reducing such a beam will be difficult to be used for measurements. In general, a positron beam can be characterized by the beam brightness defined as $B = I_{e^+}/\left(D^2\Theta^2 E_{\|}\right)$, where D is the beam spot diameter, Θ is the angular divergence and $E_{\|}$ is the longitudinal positron energy [80]. The brightness obeys Liouville's theorem, which states that the phase space volume occupied by an ensemble of non-interacting particles keeps constant under the influence of conservative forces. This theorem is of great importance. It implies, that the minimal diameter, which can be obtained by focusing a beam, is determined already by the properties of the source, because there the inherent size of the phase space volume is defined. For electrons the usage of apertures and energy filters to reduce the phase space volume is rather common. Such optics does not violate Liouville's theorem, because with them non-conservative forces are introduced into the system. Due to the significant intensity loss when using apertures or energy filters they are not suitable for enhancement of the positron beam brightness. However, for positrons there is a method to overcome the restrictions, arising by the Liouville's theorem, the so called re-moderation. Short description is that the primary beam slow positrons are accelerated to few keV energy and focused on a moderator material. Then re-moderated positrons can be extracted from moderator either from the incident side (reflection geometry, realized at NEPOMUC [13]) or from the transmission side (transmission geometry, realized at AIST [81]). In both cases the reported efficiency in terms of intensity maintaining was about 6%, but recommendations are given for further improvement upwards the theoretical limit of

40% in case of using W. We have investigated by GEANT4 simulations the moderation efficiency in terms of maintaining the beam intensity for both geometries. The results are represented in Fig. 42. The technical implementation problems for the reflection mode is that the primary and re-moderated beams have to pass the same optics and to be separated while for the transmission mode they are related to the thickness of the moderation foil.

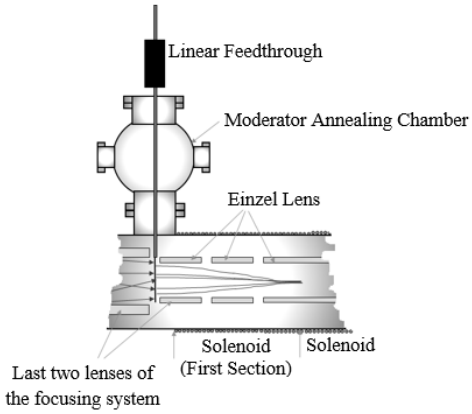

Fig. 43 – Scheme of the re-moderation stage consisting of W moderator mounted on linear feedthrough, annealing chamber and Einzel lenses. The first section of the solenoid will be powered off when re-moderator is at active position. This will provide magnetic field free volume for the Einzel lenses to act properly.

At NEPOMUC and at AIST the primary beam is first magnetically guided then extracted from the guidance magnetic field and afterwards re-moderated. We propose to build a re-moderation stage integrated with the focusing system (Fig. 39) to avoid extraction from the transportation magnetic field. As can be seen in Fig. 40 the best focusing before entering the magnetic field occur between lenses 5 and 6 which are the last two lenses of the primary beam focusing system. At this position we propose to introduce the moderator foil for transmission mode. The scheme is presented in Fig. 43. It consists of a W moderator mounted on liner feedthrough, an annealing chamber and Einzel lenses. The principle of the operation is that if the slow positron intensity is preferable for the measurements, the moderator will be out of axis, the first solenoid section will be powered on and the potentials applied to lenses will correspond to those for the focusing system. Thus the focusing system will act without re-moderation and as it was already simulated (see Fig. 40). In case the beam brightness is important, by the linear feedthrough the moderator foil will be moved on the working position, the first solenoid stage will be powered off, and the potential of the three cylinders will be set to act as Einzel lenses.

The de-magnification factor strongly depends on the energy spread of re-moderated positrons which is a function not only of the chosen material but also on the surface quality (a bumpy foil leads to a broad energy spread), the extraction fields, the surface contamination (inelastic scattering) and the degree of thermalization (epithermal positrons). The annealing quality for removing the defects is important for the re-moderation efficiency. Therefore, a chamber for *in situ* annealing and surface cleaning of the re-moderator has to be used. The de-magnification can reach 50 times [81].

3.5 ADVANCED CONCEPT FOR BEAM FORMATION

In this chapter we present an idea which can work either in direction of beam spot size reduction, by length segmentation of a fixed length converter, or of intensity increase, by using few converters with a fixed length. The idea uses the γ-beam time structure (Fig. 1) which is almost preserved (the width of the bunches is expected to be widen up to 5 ps due to the thermalization process of the fast e^+) during the pair production in the target and during the e^+ moderation.

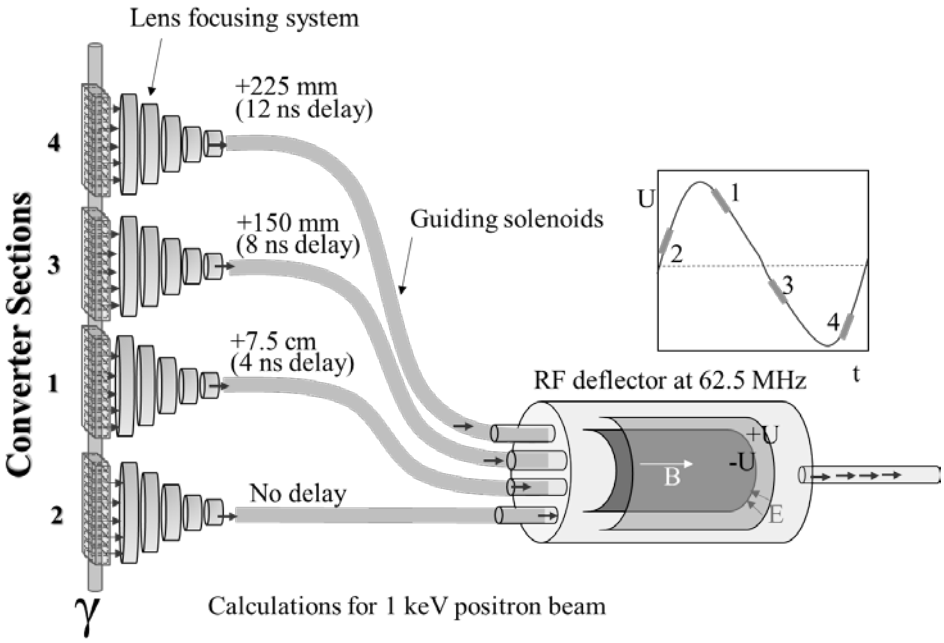

Fig. 44 – Scheme of segmented converter with a RF deflector for beam combination.

We propose to segment the converter, in length, in few sections (for example in 4, as shown in Fig. 44). Then, 4 beams are formed, as explained in the previous section, each with 4 times smaller spot diameter (compared with the case when a full length converter is used). These beams will be combined together by delaying bunches from each consequent section by 4 ns. This technique is known in electron accelerator physics as frequency multiplication by beam combination with RF cavity deflector [82]. In case the e_S^+ are extracted with $E_+ = 1$ keV, then the necessary delay can be achieved simply by a difference of 7.5 cm between the guiding tubes lengths. Special attention has to be paid on designing the deflector, which will work as e^+ -beam combiner. We propose this RF deflection cavity to be based on a $E \times B$ filter with cylindrical plates, which does not suffer from optical aberrations and the incoming profile of the beam spot preserved after the deflection [83]. With such a system and with a converter length of 30 cm we expect to have a beam spot of 12 mm for the primary slow positron beam.

3.6 BEAM TRANSPORT AND CONTROL

The e^+, as a charged particle, responds to the application of electromagnetic fields. This can be used to guide a e^+-beam adiabatically over large distances. Solenoids windings will be mounted on the beam tubes to create longitudinal field which guides the e^+ magnetically to the experimental areas. Mainly standard tubes of two different diameters corresponding to DN 63 CF and DN 100 CF will be used. The corresponding lengths are 12.5 m and 8.5 m. The length and wire type that will be used for the transport system is summarized in Table 4.

Table 4

Summary for copper wire to be used for solenoid beam transport.

Type	Solenoid length	Wire Layers	Wire Diameter (mm)	Wire Length (m)	Current density (A mm^{-2})	Magnetic field along beam axis (mT)
Solenoid 63CF	12.5 m	2	2	1394	0.86	6
Solenoid 100CF	8.5 m	2	2	1480	0.86	6
Small Helmholtz coil R=34 mm	20×(0.1 m)	3	2	30×20	1.6	6
Large Helmholtz coil R=52 mm	8×(0.05 m)	3	2	16×8	1.6	6

Where the geometry of the transport line would require several large gaps in a solenoidal coil design, a Helmholtz coil configuration is needed. A current density of 1.6 A mm^{-2} was assumed in the Helmholtz coils, with 0.86 A mm^{-2} current density for the solenoid beam line, with a resulting strength of about 6 mT (60 G). The Helmholtz coils will be placed along the tube, at the position of the flanges and pneumatic vacuum gate valves. Large Helmholtz coils will be used for the experimental chambers. A solenoidal magnetic field can be used for adiabatic beam

transport even if the field has small perturbations or even if the solenoid is bent with a sufficient large radius. The latter case, however, leads to the curvature and gradient drift which have to be corrected by appropriate saddle coils mounted transversal to the solenoid axis. These are also needed in order to compensate small constant disturbances of the beam.

A few beam switches will be used in order to deliver the beam at the experimental setups. Adiabatic magnetic beam switches are successfully used in the NEPOMUC laboratory [84]. The design does not require extraction from the longitudinal magnetic guiding field. The simplest approach is the superposition of the longitudinal main field generated by a solenoidal coil with a transverse switching field by a magnetic dipole. The field is provided by a μ-metal core which extends over the middle third of the switch, with the coils wound on the core. Simulations by COMSOL have shown only a slight deformation of the momentum density distribution of the phase space volume after the beam deflection [84]. This is caused mainly by the deviation from uniformity of the longitudinal magnetic field strength, especially at the entrance and at the exit of the beam switch.

Other types of beam switches can be realized by mechanical rotation of a Helmholtz coil or by using an $E \times B$ filter with cylindrical deflection plates (similar to the beam combiner shown in Fig. 44).

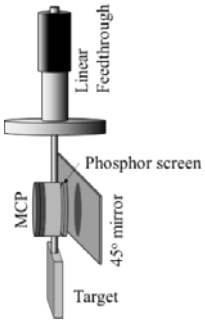

Fig. 45 – Schematic of a linear feedthrough with MCP coupled with phosphor screen to be used as a beam monitor.

The beam control will be achieved by micro channel plate (MCP) coupled with a phosphor screen, its reflection being recorded by a CCD camera trough a view port and a 45° mirror (Fig. 45) [85]. The MCP and the Al target will be mounted on a linear feedthrough which will allow either to align the MCP to the beam axis, for visual control, or the target, for counting purposes, with an external detector for 511 keV γ-ray (or to be used as anode for charge collection) for beam controlling and tuning, or to leave the beam path free at e^+-beam working condition.

Without beam, a ^{22}Na-calibration source encapsulated in Al can be mounted at the target position in order to record an annihilation spectrum with known intensity with the same experimental constraints of the external detector. Hence, systematic errors such as attenuation in the stainless steel wall of the beam line or Compton scattering in the lead shielding could be minimized.

3.7 COINCIDENCE DOPPLER BROADENING SPECTROSCOPY

The sample chamber for CDBS is schematically shown in Fig. 46. The design copies some of the functionality of the NEPOMUC CDBS chamber. The difference in the design proposed in Fig. 46 is that the positrons are guided magnetically to the sample and no focusing is applied.

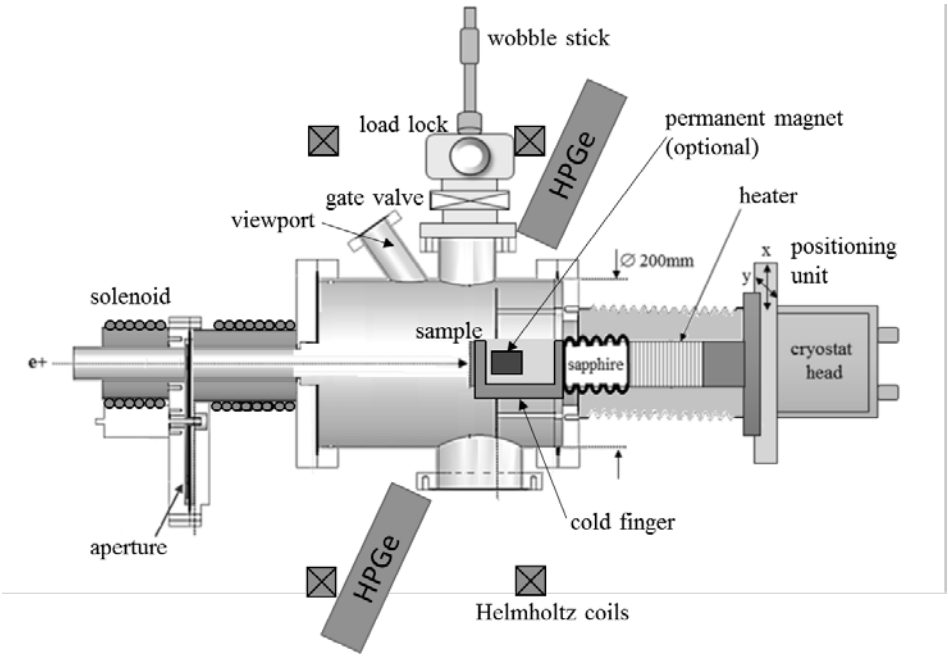

Fig. 46 – Sketch of the sample chamber of the CDBS.

In the original NEPOMUC design a magnetic field termination is followed by a system of electrical lenses used for focusing the beam spot on the sample. It has to be mentioned that such setup most probably will affect the polarization degree of the positrons due to strong fringing effect of the magnetic termination μ-metal flange and this is the reason we propose a more simple design without extracting the slow positrons out of the guiding magnetic field. The variable aperture is mounted inside the vacuum and manipulated via a rotary feedthrough from atmosphere. By selection

of the aperture a desired part of the positron beam can be shielded and the beam diameter at the entrance of the focusing system will be adjustable. The variable aperture causes a strong background radiation if a borehole with a small diameter is used to reduce the beam size at the entrance of the lens system. It is therefore favorable to increase the distance of the aperture from the sample in order to keep the aperture induced background in the detectors as small as possible. If spin polarization is not important for the measurements, focusing of the beam can be achieved by placing a permanent magnet fixed at the beam axis position (see Fig. 46), without contact with the cold finger.

The sample station can be moved in *x*- and *y*- direction perpendicular to the beam axis (with step motors in order to perform two dimensional scans). A potential behind the sample has to be installed in order to homogenize the potential landscape and to make it independent from the position of the sample.

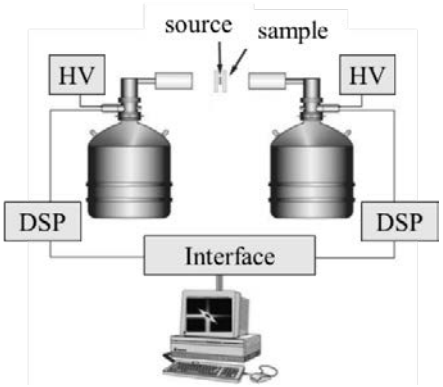

Fig. 47 – Schematic of a CDBS spectrometer. HV - high voltage power supplies, DSP - digital signal processing. The interface is to register the energies of the two annihilation quanta.

The sample station of the CDBS has to meet five requirements. Firstly, it should be movable in the vacuum system in order to perform two dimensional scans. Secondly, it has to be insulated to apply an acceleration voltage down to −30 kV for adjusting the positron energy and hence the positron implantation depth. Thirdly, a sample cooling/heating is necessary in order to investigate materials with shallow traps and fourthly only very small amounts of structure material should attenuate the annihilation radiation on its way to the HPGe detectors. The sample holder is manufactured from copper to ensure a good thermal coupling to the cryostat. The electrical insulation is demanding in terms of heat conductivity. A sapphire insulator have to be constructed which will ensures a good thermal contact at low temperatures on the one hand and insulates electrically on the other hand. The fifth requirement is easy and fast sample exchange. This will be realized by the help of a load lock and a wobble stick.

The detectors setup consists basically of two HPGe detectors aligned in collinear geometry (Fig. 47). The signals are read either by Digital Signal Processor units (DSP) or digitizers and stored, event by event, in a two-dimensional array. The energy resolution of these Ge detectors is about 1.2 keV (FWHM). Using conventional β^+ sources, the distance between the source and each of the detectors is about 20-30 cm which is limited by the HPGe detector count rate of 2×10^4 s^{-1} in order to sustain reasonable dead time due to pile up. In such a setup, a final count rate of less than 500 s^{-1} is usually obtained in the 511-keV peak by using a 40 μCi β^+ source. About 1×10^7 events should be collected in the two-dimensional spectrum. However, in some cases in order to reveal small differences the statistics had to be increased to be about 5×10^7.

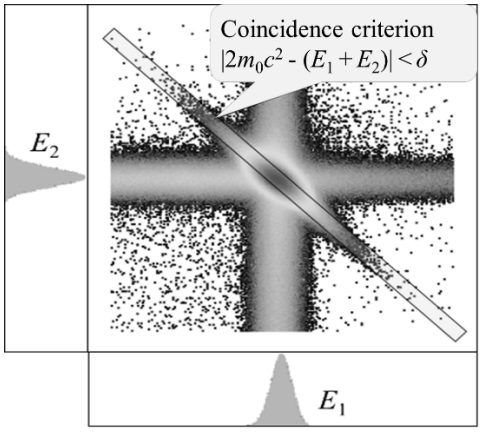

Fig. 48 – Two-dimensional CDBS spectrum with the energy criterion for true coincidence.

Using two HPGe the aim is to detect the energies E_1 and E_2 of both annihilation γ-quanta which originate from the same annihilation event. The sum energy $E_1 + E_2$ then equals $2m_0c^2 - E_B$, with E_B being the binding energy of the e^- and e^+ in the solid. The difference energy $E_1 - E_B$ is equal to $p_L c$ with p_L being the momentum component of the annihilating pair in the direction of the detector 1. The energy of the detected γ-quanta is then red (blue) Doppler-shifted by an amount of $\pm p_L c/2$ (see *e.g.*, Refs. [32, 30]). The essence of the method lies in the possibility to take a diagonal cross-section of the two-dimensional spectrum considering only of events which fulfill the condition $E_1 + E_2 = 2m_0c^2$ (Fig. 48). The result is practically a background-free, symmetric spectrum. A peak to background ratio of approximately 10^6 was found (Fig. 49) in agreement to other results [30]. No further attempt was necessary to remove the remaining background which was found to have only negligible intensity. This background is mainly due to the Compton scattering of the

1.28 MeV γ-quanta from the β^+ source. Thus, it will be further reduced in a e^+-beam system where the 1.27 MeV γ-quanta are not present.

A cross-section along the other diagonal $E_1 - E_2 = 0$ gives a good approximation of the energy resolution ΔR of the system [30]. In practice, the cross-section is taken within a small width δ according to $2m_0c^2 - (E_1 + E_2) < \delta$. The optimum width of the cross-section must be optimized because a too small δ will waste statistics, whereas a too high δ will fail to remove all the unwanted background. Folding is equivalent to an improvement of the statistics by a factor of two.

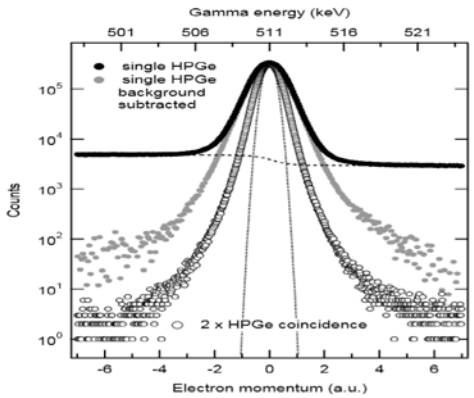

Fig. 49 – Comparison of Doppler spectra as obtained by CDBS and with a single HPGe detector. Reproduced with permission from [86].

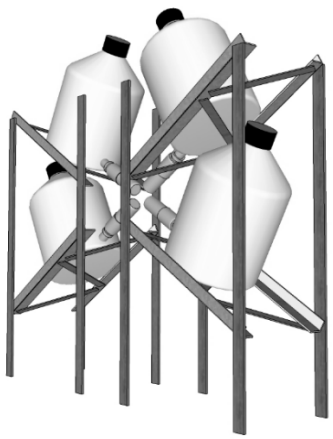

Fig. 50 – Arrangement of two couples of HPGe detectors with 30 L dewars.

In order to double the count rate we propose using of two couples of HPGe detectors. Each couple is configured to work as a CDBS spectrometer. Possible arrangement of the four HPGe detectors equipped with 30 L dewars is shown in Fig. 50.

3.8 POSITRON ANNIHILATION LIFETIME SPECTROSCOPY

3.8.1. Secondary electrons for tagging

The PALS with a e^+-beam can be achieved by using the detected secondary electrons which are kicked out from the sample by the incident e^+ [87, 88]. There are different ways to design such technique. We propose a setup which has been built in two laboratories and demonstrated excellent performance with time resolution better than 500 ps (FWHM) and excellent peak to background ratio better than 10^5 [89, 90]. The secondary electrons in this setup are detected by an fast MCP and the signal is used as a start signal for the PALS spectrometer. Specially designed $E \times B$ filter made of three sets of parallel plates are used to decouple the e_S^+-beam from the secondary electrons and to guide the secondary electrons to the MCP independently from the acceleration energy of the e_S^+.

3.8.2. Bunching system

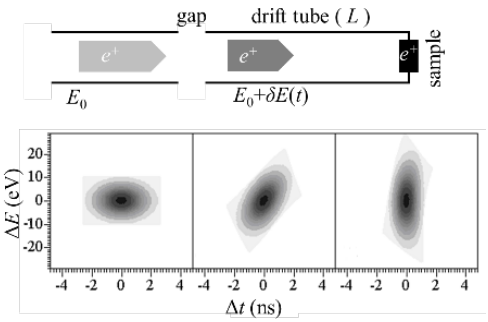

Fig. 51 – Upper part: scheme of single gap buncher. Lower part: time compression of the e_S^+ pulse.

The bunching technique is well-known and it was applied in many positron laboratories worldwide in order to developed pulsed e^+-beam from a DC e^+ source. The technique consists in modulating the longitudinal velocity of charged particles by applying a time dependent electric field to accelerate/decelerate the particles that would arrive too late/early at the time focus. The main advantage of the bunching method is that a compression in the time space is done and therefore in the ideal case

no intensity loss is observed. The upper part of Fig. 51 illustrates the working principle of a buncher. In the lower part the phase space is shown.

The ideal modulation energy $\delta E(t)$ can be described by a parabolic function:

$$\delta E(t) = E_0 \left(\frac{1}{\left(1-\frac{t}{\tau}\right)^2} - 1 \right), \tag{9}$$

where E_0 and t are the energy and the time at which e^+ enter the buncher, respectively, and τ is the transit time from the buncher to the time focus position [91]. The typical PALS spectrometer time range, suitable for a wide range of samples (excluding Ps forming materials with large pores), is 20-40 ns. This determines the operating frequency for pulsing of 25-50 MHz. At this frequency technical difficulties appear in application of the ideal shape of the modulation potential. In many cases a practical approach is to replace the ideal shape by a sawtooth approximation (see Eq. 10), or by using only the linear part of the sine function at the zero-crossing (Eq. 11). Disadvantage of the former approach is the large energy spread which will affect the final time resolution, while the last one works only on approximately 10% of the time when sinewave is approximated by linear function and the last determines a need of pre-buncher.

The modulating sawtooth potential can be written as:

$$\delta U(t) \approx (2E_0/e)(t/\tau). \tag{10}$$

For the linear part of a sine wave it can be written:

$$\delta U(t) = U_0 \sin \omega t \approx U_0 \omega t = (2E_0/e)(t/\tau), \tag{11}$$

from where the required potential amplitude is obtained:

$$U_0 = \sqrt{8E_0^3/m}/(e\omega L). \tag{12}$$

We propose the bunching system of the pulsing beam to consist of a pre-buncher, chopping, and the main buncher (Fig. 53). It will operate with double gap sinewave buncher. It is made with selecting such length of the buncher which will be passed by a e^+ for half period of the sinewave. Due to the fact that the primary beam e_s^+ will be with wide energy spread of few tens of eV it will need re-moderation in order to achieve high quality bunching.

The purpose of the pre-buncher is to reduce the losses by pre-bunching the e^+ in such a way that in the main buncher gaps most of them will arrive at the gap when acts the linear parts of the sine wave potential. Chopper is also needed due to the fact that the energy distribution of the e_s^+ is not fully symmetric. The tails in the energy distribution usually leads to complex time resolution function of the spectrometer. The chopper also improves the peak to background ratio of the PALS spectrum. Two

deflection plates will play the role of a chopper. They can work in magnetic field environment [92].

With the described bunching system the e^+ can be bunched in short pulses of approximately 100 ps and the final time resolution of the PALS spectrometer will be determined mainly by the resolution of the scintillation detector for 511 keV annihilation γ-rays.

The sample chamber will be equipped with cryostat for sample temperature control and a load lock for fast sample exchange.

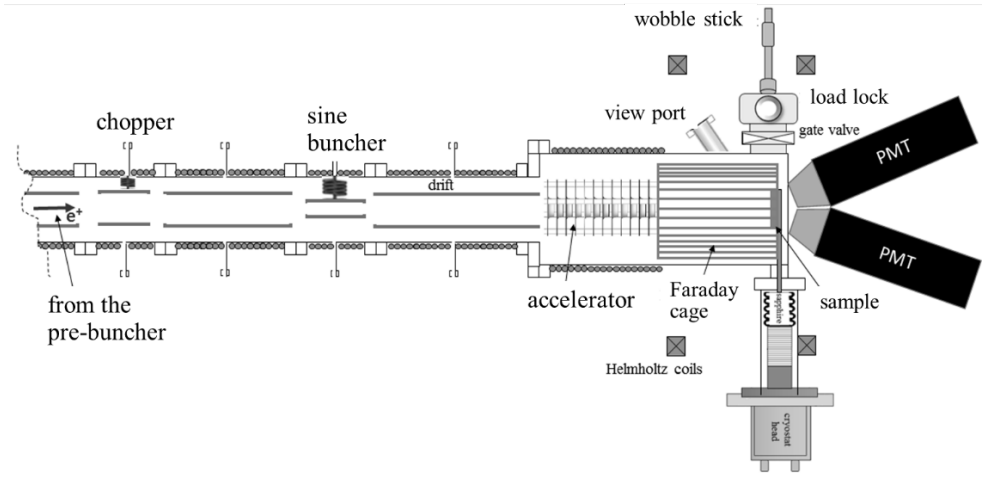

Fig. 52 – Sketch of the pulsing system with sample chamber for PALS.

3.9 AGED MOMENTUM CORRELATION SPECTROSCOPY

The four HPGe detectors of the CDBS setup will be used and only the geometrical arrangement will be different. The arrangement is shown in Fig. 54 and it will provide four independent AMOC spectrometers by which the acquisition time for a spectrum can be shorten 4 times.

The proposal is to build the AMOC spectrometer as alternative of the PALS branch of the beam line. The simplest AMOC system consists of a HPGe detector paired with a BaF_2 detector to catch the two annihilation 511 keV γ-quanta in coincidence (see Fig. 53). The start for the PALS system can be delivered either by the electronics of the bunching system or by detection of a secondary electron (see Section 3.8).

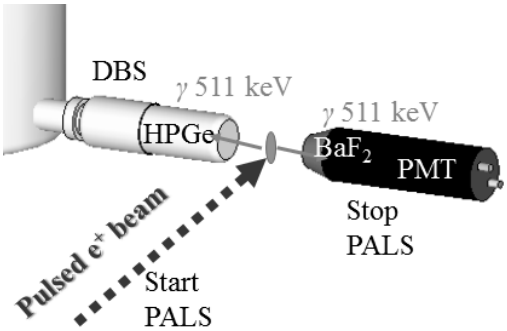

Fig. 53 – AMOC setup on pulsed e^+-beam.

Fig. 54 – Four AMOC setups to be realized on e^+-beam.

3.10 POSITRON ANNIHILATION INITIATED AUGER ELECTRON SPECTROSCOPY

The main technical requirements for sample preparation and measurements are: fast cooling of the samples, so the heating solution of the samples should allow for this; *in situ* transfer of the sample between deposition chamber and the PAES analysis chamber; the $LaAlO_3$ layer will be deposited by sequential deposition of the constituent oxides (La_2O_3 and Al_2O_3) or from single target, by sputtering, using a special on-axis, long-distance configuration (see next); special design of the sputter

chamber to accommodate *in situ*, real time, atomic scale growth control by high-pressure RHEED (Reflection High Energy Electron Diffraction).

For sample preparation we will use a deposition method that it is easy to implement, cost effective, namely sputter, in a special configuration (*i.e.*, on-axis, large distance sputtering) that will allow growth control of oxides at atomic level and, therefore, high quality interfaces. Sputtering gives also the advantage of uniform large scale deposition, considering that we foresee a sample size of $\phi = 25\text{-}50$ mm, as determined by the e^+-beam diameter that will be available at ELI-NP. This deposition method and its advantages over other thin film growth techniques (*e.g.*, pulsed laser deposition, molecular beam epitaxy, off-axis sputtering) are described in [93]. The basic idea of the method is to use a substrate-target distance larger than the mean free path of the high energetic ions that are coming from the target, allowing co-deposition or multilayer growth, by switching between different sources, and, due to the large distance (of the order of 30 cm), ensuring a more homogeneous deposition on larger substrates [93].

A schematic representation of the proposed setup for the first TOF-PAES experiments at ELI-NP is given in Fig. 55, consisting of the analysis chamber and a load lock chamber with an Ar-ion milling unit for sample cleaning and a DC/RF sputter unit for sample preparation (metals or oxides). The vacuum chambers are interconnected for *in situ* manual transfer of a sample between the deposition and the analysis chambers. The main components foreseen for each chamber are described below:

Chamber 1 with the role of a load lock, dry etching by means of plasma/ion-milling for sample cleaning, and sample preparation by RF/DC sputter. Main components: a plasma/Ar ion-etching source; sample holder, with rotation during etching and cooling; one quadrupole mass spectrometer for controlling the etching process; one tilting RF/DC sputter source (5 cm in diameter) for sample preparation (mainly oxides); sample holder with heating solution for reaching up to 1000 ºC (for sample preparation, for improving the surface crystallinity, degassing, *etc.*); required background pressure less than 1×10^{-8} mbar; handling of samples up to 5 cm in diameter. Optional, an e^--beam evaporation unit for metallization can be added, at the base of the chamber and separated from the sputter deposition chamber by a valve, for protecting the samples in case of their transfer for studies with other e^+ analysis tools at ELI-NP.

Chamber 2 with the role of analysis chamber by means of (TOF-)PAES and AES (Auger Electron Spectroscopy). The proposed main components for this chamber are: e^--beam gun for AES; NaI scintillator for monitoring the e^+ flux by measuring the number of annihilation γ-rays; a Reflection High Energy Electron Diffraction (RHEED) unit for checking the sample surface crystallinity before PAES analysis; sample holder, with sample rotation, tilting, and heating (for removal of surface contamination); handling of samples up to 5 cm in diameter; required background pressure less than 1×10^{-10} mbar.

The advantages of the proposed TOF-PAES setup over existing analysis tools:

– it gives the possibility to do the studies *in situ*, with no degradation of the surface by exposure to *ex situ* conditions;

– it gives the possibility for a direct correlation between defects network and the growth front, a study that is not possible with the existing methods;

– because the PAES study is done after sample preparation, by *in situ* transfer between the preparation and the analysis chamber, it eliminates (or, at least, it reduces) the possibility of degraded interface properties, due to the presence of absorbates when the samples are exposed to *ex situ* conditions.

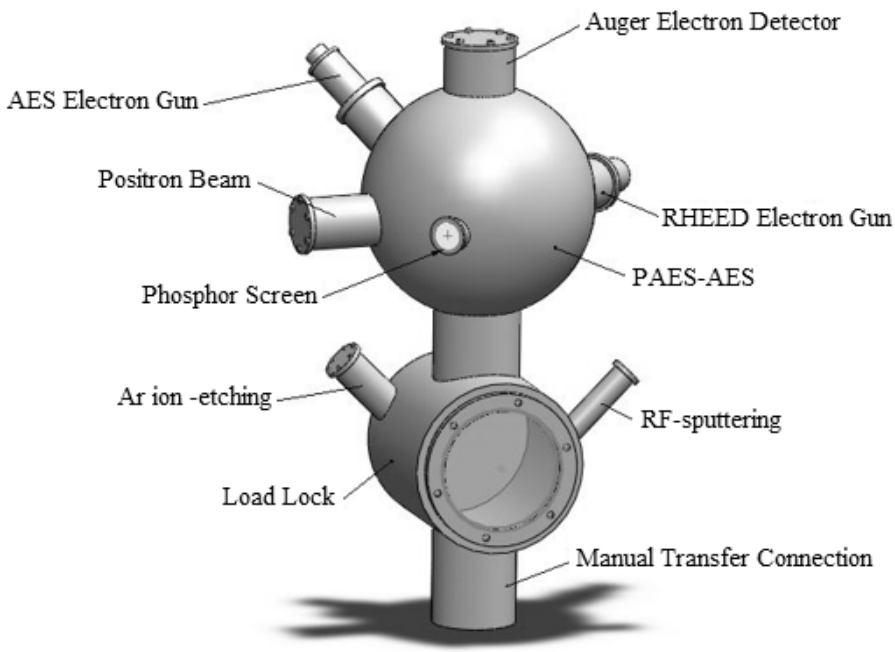

Fig. 55 – Schematic representation of the setup proposed for the TOF-PAES experiments at ELI-NP.

The TOF-PAES analyzer will be built in collaboration with the group of Dr. Christoph Hugenschmidt from Technical University of München, FRM II, based on an existing setup [49]. Development of a new type of TOF-PAES detector is foreseen after the initial step (of proving the method feasibility) in order to improve the detection of produced Auger electrons.

3.11 GAMMA-INDUCED POSITRON SPECTROSCOPY

The γ-rays from the incident γ-beam which do not interact with the converter in the vacuum chamber will pass through a thin window to go into air; the sample, held by a thin cord, is placed in the path of these γ-rays.

The proposed GiPALS system will consist of six or eight detectors (see Fig. 56) which will register annihilation photons emitted from the sample. The barium fluoride (BaF_2) crystal (mounted on PM tube Hamamatsu H3378-50 or XP2020Q) will be used to measure the time of γ-rays detection and to provide stop signals for the PALS. The signal acquisition will be fully digital, which allow the detectors to work in single channel mode or in coincidences for each 3 couples (a detector with an opposite counterpart forms a couple) to catch simultaneously both annihilation γ-rays of an annihilation event.

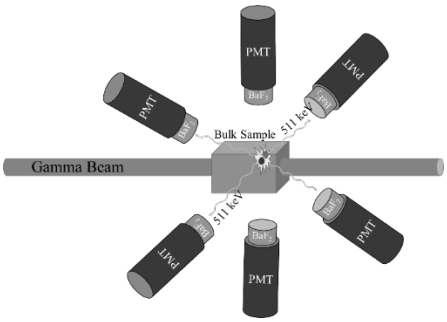

Fig. 56 – Simplified scheme for detectors setup for GiPALS, consisting of six BaF_2 detectors.

4. ESTIMATE OF COUNT RATES/FEASIBILITY OF PROPOSED DEVICES

The count rates of the devices in the subsections below will be estimated for the case that the primary beam comes from the γ-to-e_s^+ converter, with an expected intensity of approximately $1\times10^6\,s^{-1}$. The summary of the count rates is given in Table 5. The details in the estimates are described in subsections below. The number of the spectra per sample, needed for depth profiling, are consider to be 20, but depending on the scientific task this number may vary. The count rates in the table are also given for the minimum number of detectors needed for the corresponding experimental setup. The multi-detector factor shows how many times the count rates can be improved according to the multi-detector systems considered in the technical proposal.

It has to be mentioned that in case the CMA is realized with holes (2.5 mm) option (see Section 2.1.5) the spectrometers count rates will be 82% of the data given in Table 5.

Table 5

Summary for count rate estimates.

System	Version	Count rate (s^{-1})	Spectrum statistics (counts)	Time per Spectrum (min)	Time per Sample (min)	Multi-detector factor
PALS	SE tagging	7×10^3-35×10^3	2×10^6	1-5	20-100	4
	Bunching	7×10^3	2×10^6	5	100	4
AMOC		3×10^3	10^7	60	1200	4
CDBS	Coincidence	1×10^3	10^7	160	3200	2
	as DBS	2×10^4	10^6	8	160	4
GiPALS		32	10^6	520	520	3
PAES		0.03 - 0.3	10^2 - 10^3	600	600	not applicable

4.1 PALS

The first PALS method (see Section 3.8.1) we propose to be implemented is to use secondary electron tagging for start signal of the PALS. The count rate of such system is material and energy dependent as the number of the kicked out secondary electrons per e^+ is dependent on the sample material and on the incident e^+ energy. Using the data from ref. [89] the start signal rate is estimated to be 0.5 to 0.1 per e^+, *i.e.*, 1×10^5-5×10^5 s^{-1}. The stop signals will be provided by a BaF_2 detector (Ø5 × 5 cm^3), placed at a distance of 2 cm from the target. Taking into account the acceptance space angle and the intrinsic efficiency of such crystal (90%), we estimate the stop detector efficiency to catch one of the annihilation γ-rays at 7%, equivalent to a count rate of 7×10^5 s^{-1}. However, it should be mentioned that the actual rate to be obtained by a single PM detector is much smaller. It is due to the fact that the photomultiplier tube has a maximum average current (for the XP 2020: 200 μA; for good stability only 10 μA). This limits the maximum number of detected γ-quanta to about 5×10^4 s^{-1}. A possible way to increase the PM count rate is to disconnect the last dynodes of the PM and to use a fast preamplifier instead, or digital signal processing of the dynode signal. This reduces the problems with power dissipation in the PM distinctly. Thus the final PALS count rate can be estimated to 7×10^3 - 35×10^3 s^{-1}. For usual PALS spectrum statistics of 2×10^6 counts, the time for a spectrum to be measured is estimated to 1-5 min. For a depth profile study of a sample at most 20 values for the incident E_+ are necessary. Thus, a depth profiling time will be of 20 - 100 min per sample. Improve of the count rate can be achieved by stopping the multi-detector system.

The second PALS method (see Section 3.8.2) uses start signal from the electronics master frequency (50 MHz) which forms short e^+ pulses by bunching. This system needs a re-moderation stage and about 20% of the primary beam will be used for bunching. The e^+ transmission quality of the bunching system depends strongly on the way the pre-buncher is realized. The typical transmission efficiencies of the pulsed e^+-beams build in the world up to now is 50%. Consequently, we may expect the intensity of e^+ that will reach the sample to be of about 1×10^5 s^{-1}. Supposing that the stop detector system will be the same as described in the previous paragraph, 5 min is estimated to be necessary to collect a PALS spectrum.

4.2 CDBS

The γ-beam based e^+ source may provide a very large number of e^+, of approximately 10^6 s^{-1}. However, the existing detectors can only register a limited number of events. For the HPGe detectors, which will be used at ELI-NP, this is due to the extended dead time. Moreover, the number of events to be detected must be further reduced to about 2×10^4 s^{-1} to avoid detector overload, pile-up effects, and worsening of the energy resolution. This count rate can be achieved with a HPGe detector (for the calculations we consider a detector with relative efficiency of 25%) placed at the distance of 10 cm from the sample. Therefore, only by adjustment of the target to detector distance one may limit the overload and pile-up effects. The second detector of a coincidence system will reduce the count rate of the system by its own detection efficiency which is of the order of 1% absolute efficiency (at 25 cm) or approximately 6% at 10 cm. Thus, only a count rate of about 1×10^3 s^{-1} will be available. Since the comparison of experimentally observed high-momentum spectra with corresponding calculated spectra requires a high statistics (greater than 10^7 counts per spectrum), the Doppler-coincidence technique cannot be applied as a standard technique simultaneously with PALS, which will be much faster (see Section 2.4). However, for many applications the recording of “normal” (non-coincident) Doppler spectra will be very useful. This gives two independent Doppler spectra with a total count rate of about 4×10^4 s^{-1}. Since an analysis of these spectra using simple line shape parameters requires only a medium spectra statistics (about 10^6 registered events), the collection time will be rather short. Thus, the measurement automation system should allow lifetime measurements without Doppler-broadening experiments for highest data rates, and lifetime spectroscopy correlated either with coincident or non-coincident Doppler-broadening spectroscopy. Further, the overall count rate of the Doppler system can be increased by the establishment of a multi-detector arrangement of Ge detectors. We propose using of two sets of CDBS system, *i.e.*, four HPGe detectors.

4.3 AMOC

The AMOC detector setup will consist of one BaF_2 detector (Ø5 × 5 cm^3), placed at a distance which limits the maximum number of detected γ-quanta to about 5×10^4 s^{-1} (see the explanation in Section 0) and a HPGe detector at approximately 10 cm from the sample with absolute efficiency at this distance of approximately 6% (see Section 4.2). Thus the AMOC count rate (the two detectors in coincidence) is expected to be 3×10^3 s^{-1}. Using four AMOC setups it will be equivalent to 1.2×10^4 s^{-1}.

4.4 TOF-PAES

The time-of-flight spectrometer is designed so that it should allow short measurements time for the PAES spectra, by collecting the Auger electrons emitted in a solid angle of 2π around the sample (as compared with a solid angle of about few percent for classical hemispherical or cylindrical energy analyzers) [48, 49]. The electron time-of-flight is considered the time between the annihilation radiation at the sample and when the electron hits the detector [49]. While the main drawback of PAES is the low intensity of the e_s^+, the flux being five to eight orders of magnitude lower than the electron current of an electron gun [49], in case of TOF-PAES the main drawback is the low energy resolution (*e.g.*, 2 eV at $E_+ = 60$ eV). The energy analyzer of the TOF-PAES spectrometer proposed by Hugenschmidt *et al.* [49], which will be used at ELI-NP, consists of a trochoidal filter, a flight tube and a MCP to act as electron detector, designed so that it can achieve an improved energy resolution of approximately 1 eV at high electron energies up to approximately 1000 eV [94].

4.5 GiPALS

The γ-rays which will pass through the γ-to-e_s^+ converter chamber will be more than 20% of the incident γ-rays. In a target 60% of them will be able to produce e^-e^+ pairs. Consequently we may consider that in a long bulky sample (120 $cm^2\,g^{-1}$ to stop 99% of the γ-rays) about 6×10^8 e^+s^{-1} will be created. The time structure consists of 3200 bunches s^{-1} which results in approximately 2×10^5 e^+ per bunch. Keeping in mind that the bunch length is only 1 ps it will give a high overload and pile-up to the fast scintillation detectors. However, by adjusting the aperture of a collimator for the incident γ-rays and also by adjusting the distance between the sample and the detectors, or by using absorption foils, one can reduce the load to the detectors to a value close to 3200 detections per sec, in other words to detect annihilation of one e^+ per bunch. Therefore, the individual scintillation detectors count rate will be limited to 3200 s^{-1}. Considering a distance detector-sample of 10 cm and BaF_2 crystal of size Ø5 × 5 cm^3 the absolute efficiency of the detector will be

approximately 1%. So, in coincidence mode the count rate of two scintillator detectors is estimated to be only 32 s^{-1}. For statistic of 1×10^6 counts in a PALS spectrum about 10 h per spectrum will be needed.

5. CONCLUSION

The intense low-energy γ-beam of ELI-NP opens a unique possibility to produce an intense beam of moderated positrons by the (γ, e^+e^-) reaction. In this TDR we have reported the conceptual and technical design for a project of a source of polarized high intensity slow positrons with beamlines and spectrometers. We have presented design of converter/moderator assembly, made of tungsten foils. By simulations of GEANT4 we have simulated the conversion of γ-rays to fast e^+, their moderation, and, by COMSOL, the extraction of the moderated e^+ from the CMA. Optimization of the CMA sizes against obtaining a high-intensity slow e^+-beam has also been achieved. The foreseen γ-beam intensity of $2.4\times10^{10}\,\gamma\,s^{-1}$, with energies up to 3.5 MeV, determines the estimates of the primary slow positron beam intensity of 1×10^6- 2×10^6 $e_s^+s^{-1}$. Using fully circularly polarized γ-beam we would be able to obtain an intense, polarized positron beam with a polarization degree of 31-45%, a higher degree of polarization would also be possible with reduced beam intensity. We have described the basics of the positron annihilation technics PALS, DBS, CDBS, AMOC, PAES, and GiPALS, and the physical cases which they cover. The count rates of the proposed spectrometers have been estimated.

The ELI-NP facility will be user-dedicated and unique for positron research in the Eastern Europe. It will provide a simple source setup, with easy access for upgrades of the converter/moderator assembly toward more sophisticated setups, providing a more intense and brighter positron beam. The beam will have the world highest intensity of polarized positrons for material science studies and, therefore, it will become a unique tool for the investigation of magnetic samples.

Acknowledgements. N.D., S.B., V.L., A.O., and C.A.U. were supported by the Project Extreme Light Infrastructure - Nuclear Physics (ELI-NP) - Phase I, a project co-financed by the Romanian Government and European Union through the European Regional Development Fund.

REFERENCES

1. C. D. Anderson, Phys. Rev. **43**, 491 (1933).
2. C. D. Anderson, Nature **133**, 313 (1934).
3. R. Krause-Rehberg and H.S. Leipner, *Positron annihilation in semiconductors. Defect studies*, Springer series in solid state science, Vol. 127, Berlin, 1999.
4. H. Stoll, M. Koch, K. Maier, and J. Major, Nucl. Instrum. and Meth. **B 56/57**, 582 (1991).
5. G.P. Karwasz, A. Zecca, R.S. Brusa, and D. Pliszka, Journal of Alloys and Compounds **382**, 244 (2004).
6. B. Strasser, C. Hugenschmidt, and K. Schreckenbach, Mat. Sci. Forum, **363-365**, 686 (2001).

7. Groden R. Gilmore, *Practical gamma-ray spectrometry*, 2nd edition, 2008.
8. T. Omori, M. Fukuda, T. Hirose, Y. Kurihara, R. Kuroda, M. Nomura, A. Ohashi, T. Okugi, K. Sakaue, T. Saito, J. Urakawa, M. Washio, and I. Yamazaki, Phys. Rev. Lett. **96,** 114801 (2006).
9. C. Hugenschmidt, K. Schreckenbach, D. Habs, P. G. Thirolf, Appl. Phys. **B 106,** 241 (2012).
10. O. Adriani *et al.*, Technical Design Report, EuroGammaS proposal for the ELI-NP Gamma beam System, arXiv: 1407.3669v1 (2014).
11. http://www.eli-np.ro/documents/ELI-NP-GBS-Specifications-rev3-1.pdf
12. R.H. Howell, R.A. Alvarez, and M. Stanek, App. Phys. Lett., **40,** 751 (1982).
13. Christian Piochacz, Dissertation, Technische Universitat Munchen (2009).
14. H. Schut, A. van Veen, C.V. Falub, J. de Roode, and F. Labohm, Mat. Sci. Forum, **363-365,** 430 (2001).
15. C. Hugenschmidt, H. Ceeh, T Gigl, F. Lippert, C. Piochacz, M. Reiner, K. Schreckenbach, S. Vohburger, J. Weber, and S. Zimnik, Journal of Physics: Conference Series **505**, 01202 (2014).
16. K.G. Lynn, B. Nielsen, and J. H. Quateman, Appl. Phys. Lett., **47**, 239 (1985).
17. Vehanen, K.G. Lynn, P.J. Schultz, and M. Eldrup, Appl. Phys. **A 32**, 163 (1983).
18. See http://www.comsol.com
19. L.V. Jørgensen, F. Labohm, H. Schut and A van Veen, and J. Phys.: Condens. Matter **10**, 8743 (1998).
20. P. W. Zitzewitz, J. Van House, A. Rich, and D. W. Gidley, Phys. Rev. Lett. **43**, 1281 (1979).
21. J. Van House and P. W. Zitzewitz, Phys Rev **A 29,** 96 (1984).
22. M. Maekawa, Y. Fukaya, A. Yabuuchi, I. Mochizuki, and A. Kawasuso, Nucl. Instrum. and Meth. **B 308,** 9 (2013).
23. V. E. Balakin and A. A. Michailichenko, Preprint INP **79-85**, 1979.
24. P. Potylitsin, Nucl. Instrum. and Meth. **A 398**, 395 (1997).
25. H. Olsen and L. C. Maximon, Phys. Rev. **114**, 887 (1959).
26. H.A. Tolhoek, Rev. Mod. Phys. **28,** 277 (1956).
27. Helmut Wiedemann, *Particle Accelerator Physics*, Springer-Verlag Berlin Heidelberg, 2007.
28. H. J. Zhang, S. Yamamoto, Y. Fukaya, M. Maekawa, H. Li, A. Kawasuso, T. Seki, E. Saitoh, and K. Takanashi, Scientific Reports **4,** 4844 (2014).
29. Rich, J. Van House, D. W. Gidley, and R.S. Conti, Appl. Phys. **A 43**, 275 (1987).
30. M. Alatalo, H. Kauppinen, K. Saarinen, M.J. Puska, J. Mäkinen, P. Hautojärvi, and R. M. Nieminen, Phys. Rev. **B 51**, 4176 (1995).
31. C. Kruseman, H. Schut, A.v. Veen, P. E. Mijnarends, M. Clement, and J. M. M. d. Nijs: Appl. Surf. Sci. **116**, 192 (1997).
32. P. Asoka-Kumar, M. Alatalo, V.J. Ghosh, A. C. Kruseman, B. Nielsen, and K.G. Lynn, Phys. Rev. Lett. **77**, 2097 (1996).
33. U. Myler and P.J. Simpson, Phys. Rev. **B 56**, 14303 (1997).
34. R. S. Brusa, W. Deng, G. P. Karwasz, and A. Zecca, Nucl. Instrum. and Meth. **B 194**, 519 (2002).
35. F. A. Selim, D. P. Wells, J. F. Harmon, and J. Williams, J. Appl. Phys. **97,** 113539 (2005).
36. Y. Taira, H. Toyokawa, R. Kuroda, N. Yamamoto, M. Adachi, S. Tanaka, and M. Katoh, Rev. Sci. Instrum. **84** 053305 (2013).
37. M. Butterling, W. Anwand, T. E. Cowan, A. Hartmann, M. Jungmann, R. Krause-Reihberg, A. Krille, and A. Wagner, Nucl. Instrum. and Meth. **B 269**, 2623 (2011).
38. R. N. West, *Positron studies of condensed matter*, Adv. Phys. **22,** 263 (1973).
39. M. J. Puska and R. M. Nieminen, Rev. Mod. Phys., **66(3),** 841 (1994).
40. H. Nakanishi and Y.C. Jean, *Positrons and positronium in liquids*. In: Schrader DM and Jean YC, editors. Positron and positronium chemistry. Amsterdam: Elsevier Science, 159 (1988).
41. S.J. Tao, Journal of Chemical Physics **56**, 5499 (1972).
42. M. Eldrup, N.J. Pedersen, and J.N. Sherwood, Physical Review Letters **43,** 1407 (1979).
43. T. Goworek, K. Ciesielski, B. Jasinska, and J. Wawryszczuk, Chem. Phys. **230**, 305 (1998).
44. D.W. Gidley, W.E. Frieze, T.L. Dull, A.F. Yee, E.T. Ryan, and H.M. Ho, Phys. Rev. **B 60**, R5157 (1999).

45. P. Willutzki, J. Störmer, D.T. Britton, G. Kögel, P. Sperr, R. Steindl and W. Triftshäuser, Proc. SLOPOS 5, Jackson, Wyoming, 1992.
46. Y. Kishimoto, S. Tanigawa, in Positron Annihilation, P.G. Coleman, S.C. Sharma, L.M. Diana (Eds.), North Holland, Amsterdam, pp. 815 (1982).
47. T. Oka, S. Jinno, and M. Fujinami, Anal. Sci. **25**, 837 (2009).
48. S. Legl and C. Hugenschmidt, Phys. Stat. Sol. **C 4**, 3981 (2007).
49. C. Hugenschmidt and S. Legl, Rev. Sci. Instrum. **77**, 103904 (2006).
50. K. Uhlmann, W. Triftshäuser, G. Kögel, P. Sperr, D. T. Britton, A. Zecca, R. S. Brusa, and G. Karwasz, J. Anal. Chem. **353**, 594 (1995).
51. H. Weiss and P. G. Coleman, *Surface science with positrons* (Chap. 5), in Positron beam and their applications, P. G. Coleman (Ed.), World Scientific, Singapore, pp. 129-190 (2000).
52. H. Weiss, *Positron annihilation induced Auger electron spectroscopy* (Chap. 45) in Handbook of surface imaging and visualization, A. T. Hubbard (Ed.), CRC Press, Boca Raton, Florida, pp. 617-633 (1995).
53. R. Allenspach, D. Mauri, M. Taborelli, and M. Landolt, Phys. Rev. B **35**, 4801 (1987).
54. T. C. Q. Noakes, P. Bailey, and G. van der Laan, Phys. Rev. **B 67**, 153401 (2003).
55. M. Teodorescu, Surf. Sci. **601**, 4292-4296 (2007).
56. G. Popescu, M. A. Husanu, L. Trupina, L. Hrib, L. Pintilie, A. Barinov, S. Lizzit, P. Lacovig, and C. M. Teodorescu, Phys. Chem. Phys. **17(1)**, 509 (2015).
57. M. A. Husanu, D. G. Popescu, C. A. Tache, N. G. Apostol, A. Barinov, S. Lizzit, P. Lacovig, and C. M. Teodorescu, Appl. Surf. Sci., accepted (2015); DOI:10.1016/j.apsusc.2015.01.153.
58. Pancotti, J. Wang, P. Chen, L. Tortech, C. M. Teodorescu, E. Frantzeskakis, and N. Barrett, Phys. Rev. **B 87**, 184116 (2013).
59. L. E. Stoflea, N. G. Apostol, L. Trupina, and C. M. Teodorescu, J. Mater. Chem. **A 2**, 14386 (2014).
60. M. Kolpak, I. Grinberg, and A. M. Rappe, Phys. Rev. Lett. **98**, 166101 (2007).
61. N. Reyren, S. Thiel, A. D. Caviglia, L. Fitting Kourkoutis, G. Hammerl, C. Richter, C. W. Schneider, T. Kopp, A.-S. Rüetschi, D. Jaccard, M. Gabay, D. A. Muller, J.-M. Triscone, and J. Mannhart, Science **317**, 1196 (2007).
62. Makkonen, A. Snicker, M. J. Puska, J. –M. Mäki, and F. Tuomisto, Phys. Rev. **B 82**, 041307R (2010).
63. J. Edwardson, P. G. Coleman, T.-T. A. Li, A. Cuevas, and S. Ruffell, J. Appl. Phys. **111,** 053515 (2012).
64. Orlando, P. Lacovig, L. Omiciuolo, N. G. Apostol, R. Larciprete, A. Baraldi, S. Lizzt, ACS Nano **8**, 12063-12070 (2014).
65. C. G. Duan, J. P. Velev, R. F. Sabirianov, Z. Q. Zhu, J. H. Chu, S. S. Jaswal, E.Y. Tsymbal, Phys. Rev. Lett. **101,** 137201 (2008).
66. S. Andrieu, E. Foy, H. Fischer, M. Alnot, F. Chevrier, G. Krill, M. Piecuch, Phys. Rev. **B 58**, 8210 (1998).
67. V. Anisimov, V. D. Borman, and A. P. Popov, Phys. Rev. **B 49**, 3874 (1994).
68. A. Lungu, N. G. Apostol, and C. M. Teodorescu, *Basic concepts in ferromagnetism of diluted magnetic semiconductors. The case of manganese ambedded in Ge (001)* (Chap. 4) in Nanomagnetism, J. M. Gonzales Estevez (Ed.), OCP, Manchester, pp.74-110, ISBN: 978-1-910086-05-6, 2014.
69. T. Dietl, A. Haury, and Y. Merle d'Aubigne, Phys. Rev. **B 55,** R3347 (1997).
70. W. Eerenstein, N. D. Mathur, and J. F. Scott, Nature **442**, 759 (2006).
71. L. Pintilie and M. Alexe, J. Appl. Phys. **98**, 124103 (2005).
72. E. D. Cashwell and C. J. Everett, *A Practical Manual on the Monte Carlo Method for Random Walk Problems*, Pergamon, London, 1959; https://mcnp.lanl.gov.
73. R. Suzuki, T. Ohdaira, A. Uedono, Y. Koo Cho, S. Yoshida, Y. Ishida, T. Ohshima, H. Itoh, M. Chiwaki, T. Mikado, T. Yamazaki and S. Tanigawa, Jpn. J. Appl. Phys. **37,** 4636 (1998).
74. N. Owada, K. Hinode, S. Tanigawa, M. Doyama, and S. Okuda, in Proc. 5th Int. Conf. Positron Annihilation, Lake Yamanaka, (Japan Institute of Metals, Sendai), 743 (1979).

75. Amarendra, K.F. Canter, and D. C. Schoepf, J. Appl. Phys. **80**, 4660 (1996).
76. I. Hawari, D. W. Gidley, J. Xu, J. Moxom, A. G. Hathaway, B. Brown, and R. Vallery, AIP Conf. Proc. **1099**, 862 (2009).
77. J. Moxom, A. G. Hathaway, and A.I. Hawari, *Out of core testing of the North Carolina State University PULSTAR reactor positron beam*, Nuclear Science Symposium Conference Record, NSS '07. IEEE, Volume **3**, 2343 – 2348 (2007).
78. C. V. Falub, S. W H. Eijt, P. E. Mijnarends, H. Schut, and A. van Veen, Nucl. Instrum. and Meth. **A 488,** 478 (2002).
79. J. Oila, V. Ranki, J. Kivioja, K. Saarinen, and P. Hautojärvi, Appl. Surf. Sci. **194,** 38 (2002).
80. P. Mills, Appl. Phys. **23**, 191 (1980).
81. N. Oshima, R. Suzuki, T. Ohdaira, A. Kinomura, T. Narumi, A. Uedono, and M. Fujinami, J. Appl. Phys. **103**, 094916 (2008).
82. R. Corsini, A. Ferrari, L. Rinolfi, P. Royer, and F. Tecker, Phys. Rev. **STAB 7,** 040101 (2004).
83. S. M. Hutchins, P. G. Coleman, R. J. Stone, and R. N. West, J. Phys. E: Sci. Instrum. **19,** 282 (1986).
84. C. Hugenschmidt, C. Piochacz, M. Reiner, and K. Schreckenbach, New Journal of Physics **14,** 055027 (2012).
85. C. Hugenschmidt, T. Brunner, J. Mayer, C. Piochacz, K. Schreckenbach, and M. Stadlbauer, Applied Surface Science **255**, 50 (2008).
86. F. Tuomisto and I. Makkonen, Rev. Mod. Phys. **85**, 1583 (2013).
87. D. W. Gidley, K. G. Lynn, M. P. Petkov, M. H. Weber, J. N. Sun, A. F. Yee, *Depth-profiled positron lifetime spectroscopy of thin insulation films*, in: C.M. Surko, F.A. Gianturco (Eds.) New Directions in Antimatter Chemistry and Physics, The Netherlands: Kluwer Acad. Publ., Dordrecht, 151-171 (2001).
88. K.G. Lynn, W.E. Frieze, and P.J. Schultz, Phys. Rev. Lett. **52**, 1137 (1984).
89. Marinov, N. Djourelov, P. Nédélec, and L. Petrov, Nucl. Instrum. and Meth. **B 729**, 569 (2013).
90. Badertscher, P. Crivelli, A. Rubbia, A. S. Belov, N. V. Golubev, S. N. Gninenko, M.M. Kirsanov, T. Anthonioz, P. Nédélec, D. Sillou, J. Viret, N. Alberola, C. Bas, *Feasibility study of a positron lifetime spectrometer for measurements of porous and polymer films with a DC positron beam*, Preprint LAPP-EXP 2004.07/ INR-HEP-2004.30, 2004.
91. F. Lynch, R. Lewis, L. Bollinger, W. Henning and O. Despe, Nucl. Instrum. and Meth. **159,** 245 (1979).
92. L. Ravelli, *Improvement of the Pulsed Low Energy Positron System (PLEPS) for complex problems in materials science*, PhD Thesis, Universitat der Bundeswehr Munchen eingereicht (2014).
93. P. M. Leufke, A. K. Mishra, A. Beck, Di Wang, C. Kubbel, R. Kruk, and H. Hahn, Thin Solid Films **520**, 5521 (2012).
94. J. Mayer, *High energy resolution and first time-dependent positron annihilation induced Auger electron spectroscopy*, PhD thesis, Technical University of München, 2010.